UNIVERSIDADE DE
COIMBRA

Joana Inês Pires Cunha

DEVELOPMENT OF METHODOLOGIES FOR PERMEABILITY AND VESICLE FUSION EVALUATION

Dissertation presented at the Faculty of Sciences and Technology of the University of Coimbra
to obtain a Master Degree in Chemistry with specialization in Advanced and Industrial Chemistry
oriented by Professor Dr Maria João Moreno

September 2018

Faculty of Sciences and Technology of the University of Coimbra
Department of Chemistry

Joana Inês Pires Cunha

Development of methodologies for permeability and vesicle fusion evaluation

Dissertation presented at the Faculty of Sciences and Technology
of the University of Coimbra to obtain a Master degree in
Chemistry with specialization in Advanced and Industrial Chemistry

Coimbra
2018

"If I have seen further it is by standing on the shoulders of Giants."

Isaac Newton

Acknowledgments

The contributions of many different people, in their different ways, have made this important research project possible.

I would like to thank, first and foremost, my supervisor Prof. Dr. Maria João Moreno, for her support and encouragement, for the valuable advices, patience and hard work during these past years.

Professor Dr. Carlos Serpa, my co-supervisor, for our discussions and brainstorming of ideas. Professor Dr. Marta Piñeiro, for being my guide in the synthesis, allowing the use of her equipment and for all her kind words. Professor Dr. Seixas de Melo for the possibility of making experiments in his research laboratory, and Dr. Pina and Professor Dr. Luis Loura for the discussions of data.

I would like to acknowledge Patrícia Martins, Alexandre Silva and Ana Clara for their support during some experimental work.

I would like to acknowledge all my dearest friends and colleagues for their friendship.

To my parents, that even far away had been there every day to share my ups and downs during this journey.

Table of contents

Figures summary

Tables summary

List of Equations

Equation 1: $k = \frac{1}{\tau_D}\left(\frac{R_0}{r}\right)^6$

Equation 2: $EET = 1 - \frac{\tau_{DA}}{\tau_D} = 1 - \frac{IF_{DA}}{IF_D}$

Equation 3: $EET = \frac{1}{1+\left(\frac{r}{R_0}\right)^6}$

Equation 4: ${R_0}^6 = \frac{2.07}{128\pi^5 N_A}\frac{k^2 Q_D J}{n^4}\int F_D(\lambda)\epsilon_A(\lambda)\lambda^4 d\lambda$

Equation 5: $I_{LUV}(t) = \sum_{i=1}^{n} a_i e^{-t/\tau_i}$

Equation 6: $C_i(\%) = \frac{a_i\tau_i}{\sum_{i=1}^{n} a_i\tau_i} * 100$

Equation 7: $\tau_{av} = \frac{\sum_{i=1}^{n} a_i\tau_i * \tau_i}{\sum_{i=1}^{n} a_i\tau_i}$

Equation 8: $IF_{530} = IF_{530\ [NBD]total} * \frac{[NBD]}{[NBD]_{total}}$

Equation 9: $\%\ Release = \frac{IF(t)-IF(0)}{IF(\infty)-IF(0)} \text{ x } 100\%$

Equation 10: $\%\ F_{out} = a_1\left(1-e^{-k_1 t}\right) + a_2\left(1-e^{-k_2 t}\right)$

Abbreviations

Biotin-X DHPE	N-((6-(Biotinoyl)amino)hexanoyl)-1,2-Dihexadecanoyl-sn-Glycero-3-Phosphoethanolamine
CBF	Carboxifluorescein
DA	Donor-acceptor
DCC	N,N'-Dicyclohexylcarbodiimide
DDAB	Didodecyldimethylammonium bromide
DLS	Dynamic Light Scattering
DPPE	1,2-dipalmitoyl-*sn*-glycero-3-phosphoethanolamine
EDC	N-Ethyl-N′-(3-dimethylaminopropyl)carbodiimide hydrochloride
EET	Efficiency of Energy Transfer
ETA	Ethanolamine
FITC-dextran	Fluorescein isothiocyanate–dextran
FRET	Förster Resonance Energy Transfer
FT	Freeze and Thaw
GUV	Giant Unilamellar Vesicles
HOBT	Hydroxybenzotriazole
IF	Intensity of fluorescence
LPPC	Rac-α-palmitoyl-lysophosphatidylcholine
LUV	Large Unilamellar Vesicles
LUVs AD	Mixture of negatively and positively charged LUVs
LUVs BS	Mixture of biotinylated LUVs in Streptavidin solution
LUV-Mix	Mixture of LUVs
LUV-NBD	LUVs containing NBD in the membrane
LUV-NBD-Rho	LUVs containing NBD and Rhodamine in the membrane
LUV-Rho	LUVs containing Rhodamine in the membrane
MLV	Multilamellar Lipid Vesicles
NBD-DPPE	1,2-dipalmitoyl-sn-glycero-3-phosphoethanolamine-N-(7-nitro-2-1,3-benzoxadiazol-4-yl)
PBS	Phosphate Buffer Saline
POPC	1-palmitoyl-2-oleoyl-sn-glycero-3-phosphatidylcholine
POPE	1-palmitoyl-2-oleoyl-sn-glycero-3-phosphatidylethanolamine
POPS	1-palmitoyl-2-oleoyl-sn-glycero-3-phosphatidylserine
Rho-DPPE	1,2-dipalmitoyl-*sn*-glycero-3-phosphatidylethanolamine-N-(lissamine rhodamine B sulfonyl)
SUV	Small Unilamellar Vesicle

PA	Photoacoustic
PDI	Polydispersity Index
PVA	Polyvinyl alcohol
TCSPC	Time-Correlated Single Photon Counting
TLC	Thin Layer Chromatography
TX	Triton X-100

Resumo

A membrana biológica é uma estrutura complexa através da qual alguns fenómenos importantes como o transporte seletivo de moléculas ou a fusão acontecem e, por isso, as suas propriedades têm sido alvo de estudo ao longo dos anos. Na literatura é reportado que as ondas fotoacústicas (PA) aumentam a eficiência de absorção de fármacos por aplicação transdérmica.[1,2] Nesta dissertação tentou-se avaliar qual o mecanismo responsável e se envolve a perturbação da bicamada lipídica, avaliando a permeabilidade de membranas lipídicas e a fusão entre vesículas.

Para isso, foram usados modelos de membranas biológicas mais simples tais como LUVs (vesículas unilamelares grandes) e GUVs (vesículas unilamelares gigantes). Para avaliar a fusão entre vesículas, construíram-se curvas de calibração da eficiência de transferência de energia (EET) resultante da transferência de energia por ressonância de Förster (FRET). A EET foi obtida por medições de fluorescência em estado estacionário e transiente. Para promover a fusão entre as vesículas, a composição lipídica foi diversificada e duas metodologias para a obtenção da EET foram adotadas: mistura de LUVs com diferentes sondas e aplicação de ciclos de Freeze and Thaw; e utilizando diferentes percentagens de LUVs formados com as duas sondas. Neste estudo o par de sondas fluorescentes escolhido foi 7-nitro-2-1,3-benzoxadiazol-4-yl (NBD) e lissamina-rhodamina B sulfonil.

O estudo da permeabilidade foi realizado avaliando a cinética de libertação de uma molécula fluorescente (fluoresceína) encapsulada em LUVs. Tentou-se sintetizar um derivado da fluoresceína no sentido de criar uma série de moléculas de peso molecular sucessivamente maior e considerou-se o FITC-dextran (fluoresceína-isotiocianato-dextran) a de maior peso molecular. Esta molécula foi encapsulada em GUVs. O protocolo de produção de GUVs assistido por polyvinil álcool (PVA) foi adaptado de Weinberger et al.[3] Amostras de GUVs foram submetidas a diferentes testes de estabilidade de forma a otimizar condições para a aplicação de ondas PA. Por fim, o efeito das ondas PA na fusão entre vesículas e sua permeabilidade foi averiguado.

Abstract

The biological membrane is a complex structure through which important phenomena such as selective transport of molecules and fusion take part, hence why its properties have been studied over the years.

It has previously been reported that photoacoustic (PA) waves increase the absorption efficiency of drugs through transdermal application.[1,2] With this thesis it was intended to evaluate what is the mechanism responsible and if it involves perturbation of the lipid bilayer, evaluating the permeability of lipid membranes and fusion between vesicles.

For that, simpler biological membrane models such as LUVs (Large Unilamellar Vesicles) and GUVs (Giant Unilamellar Vesicles) were used. To assess fusion between vesicles, calibration curves of the Efficiency of Energy Transfer (EET) were obtained from Förster Resonance Energy Transfer (FRET). EET was evaluated from steady-state and time-resolved fluorescence measurements. To promote fusion between vesicles the lipid composition was modified and two methodologies for obtaining the EET values were adopted: mixing LUVs with different probes and applying Freeze and Thaw cycles; and using different percentages of LUVs with both probes. In this work, the donor-acceptor pair chosen was NBD and Lissamine Rhodamine B sulfonyl.

The permeability studies were done by assessing the kinetics of release of a fluorescent probe (fluorescein) from LUVs. The synthesis of a fluorescein derivative was attempted in order to create a series of molecules of increasingly higher molecular weight and FITC-dextran (fluorescein isothyocianate dextran) was considered the highest. This molecules was encapsulated in GUVs. The protocol for GUV formation was adapted from Weinberger et al. using polyvinyl alcohol (PVA) assisted method.[3] GUVs samples were subjected to different stability tests to optimize conditions for the application of PA waves.

Lastly, the effect of PA waves in the fusion between vesicles and permeability was studied.

Chapter 1:

Introduction

1.1. Importance of the biological membrane

Biological membranes play an essential role in the cellular protection as well as providing fundamental compartmentalization, differentiating the inside from the outside media and moving molecules selectively through this barrier.[4] The lipid components of the membrane form the permeability barrier, and the protein components act as a transport system of pumps and channels that allow specific molecules to enter and compounds to be removed from the cell, endowing membranes the important property of selective permeability.[5] Many mechanisms such as molecular recognition, enzymatic catalysis, cellular adhesion and membrane fusion take place in the membranes. In addition to the external plasma membrane, eukaryotic cells also contain internal membranes which are the barriers of organelles, unique in composition, structure and function.

1.1.1. Lipid bilayer

Membranes are dynamic structures[6], in which proteins are embedded to varying degrees in a fluid-like lipid bilayer, as described by Singer and Nicolson's model in 1972.[7] This dynamic property is based on the interactions among lipids in the bilayer and their individual mobility because they are not covalently anchored to one another.[8]

The lipid bilayer consists of two opposite layers of amphipathic lipids, with around 4nm of thickness, in which hydrophilic polar headgroups are directed towards the aqueous phase, interacting effectively with the hydrogen-bonding network of the water, and hydrophobic hydrocarbon chains are oriented towards the interior of the two layers.

The formation of lipid bilayers is a spontaneous self-assembly process in water, in which hydrophobic interactions are the major driving force. Amphiphiles in general tend to aggregate in aqueous solution above the critical micellar concentration because of the hydrophobic effect.[9] Water molecules are released from the hydrocarbon tails as they become secluded in the apolar interior of the bilayer and *van der Waals* attractive forces between them favor their close packing. There are also electrostatic and hydrogen-bonding attractions between the polar headgroups and water.[5]

In biological membranes, lipids can be arranged in two extreme lipid phases, gel (solid-ordered) and fluid (liquid-disordered). In the gel phase, the hydrocarbon lipid chains display an all-*trans* configuration, thus creating a compact lipid network where lipids lateral diffusion is strongly reduced. In the fluid phase, lipid chains are much less extended due to *trans-gauche* isomerisation and lateral and rotational diffusion of lipids are favored in fluid lipid bilayers. The transition between these phases occurs at the thermotropic phase transition (melting temperature). The most predominant state of lipids in biological membranes is the fluid phase.[4] The presence of high levels of cholesterol induces a highly ordered fluid phase (liquid-ordered) that shares some characteristics of both gel and fluid phases.[10] In biological membranes liquid-ordered and liquid-disordered phases can coexist spatially separately, e.g. lipid rafts, which are cholesterol-enriched gel domains.

1.1.2. Lipid composition

The major membrane lipids are classified into three main groups, namely phospholipids, glycolipids and sterols (Figure 1).

Glycerophospholipids are the main phospholipids found in biological membranes[7] (Table 1) and are composed of a glycerol backbone on which two fatty acid chains are esterified, in the stereospecific number positions *sn*-1 and *sn*-2. The carbon atom in the *sn*-3 position is attached to the phospholipid polar head group (choline, ethanolamine, serine, glycerol or inositol) linked to a negatively charged phosphate group (Figure 2). The phospholipid polar head group can be zwitterionic or negatively charged. Lysophospholipids only contain one fatty acid chain. Sphingolipids backbone is an unsaturated 18-carbon amino-alcohol called sphingosine, to which is linked a long saturated fatty acid chain. Sterols contain four fused cycles in *trans* configuration, a hydroxyl group in position 3, a double bond between the carbon 5 and 6, as well as an iso-octyl lateral chain in position 17.[5]

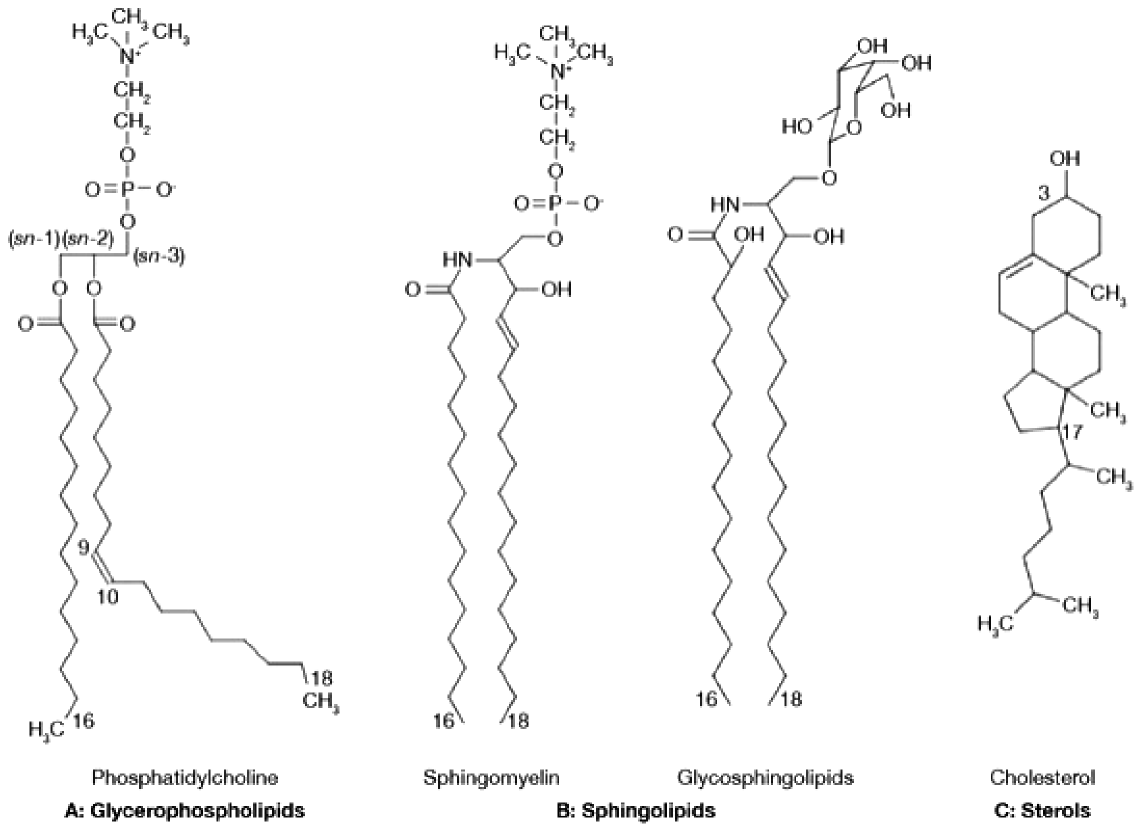

Figure 1. Chemical structures of some lipids found in biological membranes (adapted from [11])

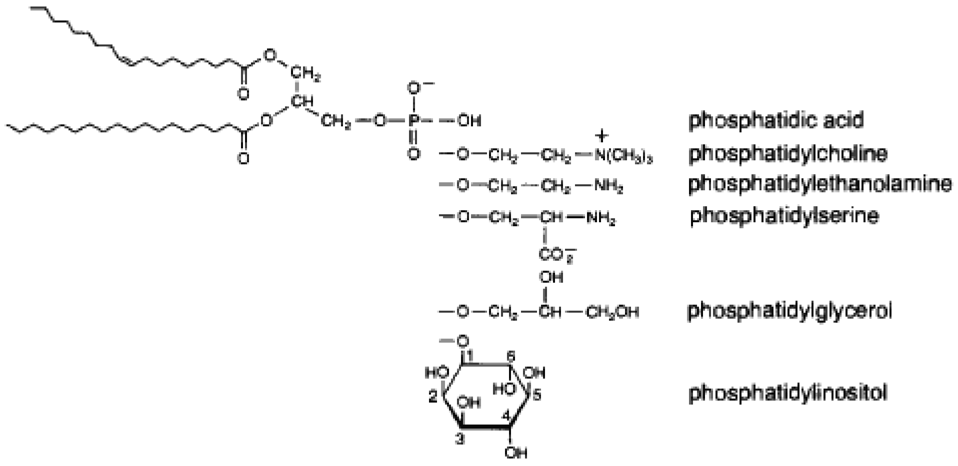

Figure 2. Phospholipid headgroups chemical structures
(adapted from [7])

In a wide variety of lipids, they can display different shapes: cylindrical e.g. PC and PS, inverted cone e.g. PE or cone e.g. LPPC (palmitoyl-lysophosphatidylcholine); or charges: neutral e.g. PC and PE, negative e.g. PS or positive e.g. DOPE (1,2-dioleoyl-*sn*-glycero-3-phosphoethanolamine). In all cells, the various phospholipids are asymmetrically distributed between the two membrane leaflets. Bacteria keep most of their negatively charged phospholipids in the outer membrane leaflet, whereas eukaryotic cells keep most of theirs, particularly PS and PE, in the inner leaflet; and SM (sphingomielin) and glycosphingolipids in the outer leaflet.[12,13]

Table 1. Major lipids in some biological membranes

(adapted from [7])

Membranes	Major lipids
Myelin (human)	PC 10% PE 20% PS 8.5% SM 8.5% Cholesterol 27%
Disk membranes (bovine)	PC 41% PE 39% PS 13%
Erythrocytes (human)	PC 25% PE 22% PS 10% SM 18% Cholesterol 25%
E. coli (inner membrane)	PE 74% PG 19% CL 3%
Sarcoplasmic reticulum (rabbit)	PC 66% PE 13% PI 8% Cholesterol 10%

Abbreviations used: PC, phosphatidylcholine; PE, phosphatidylethanolamine; PS, phosphatidylserine; SM, sphingomyelin; PI, phosphatidylinositol; PG, phosphatidylglycerol; CL, cardiolipin

1.2. Membrane properties

Besides lipids distinct physicochemical features, different lipid compositions also affect membranes properties such as melting point, phase[14], curvature, elasticity, fluidity[15], electrostatic potential[16] and permeability[17].

Membrane fluidity not only enables membrane proteins to diffuse rapidly in the bilayer plane, but it also allows membranes to fuse with one another and mix their membrane constituents with evenly distribution.[18] Membrane fluidity and permeability are strongly related, as the presence of cholesterol turns the bilayer more rigid and less permeable, while the presence of more unsaturated lipids and decreasing length chain increases the permeability.[19]

Membrane potential is a key player in many membrane-mediated phenomena such as binding of drugs or proteins to membrane surface, insertion of integral proteins and fusion of lipid bilayers.[20] The zeta potential is a scientific term for electrokinetic potential in colloidal systems, i.e., electric potential between the interfacial double layer and the dispersion medium (Figure 3).

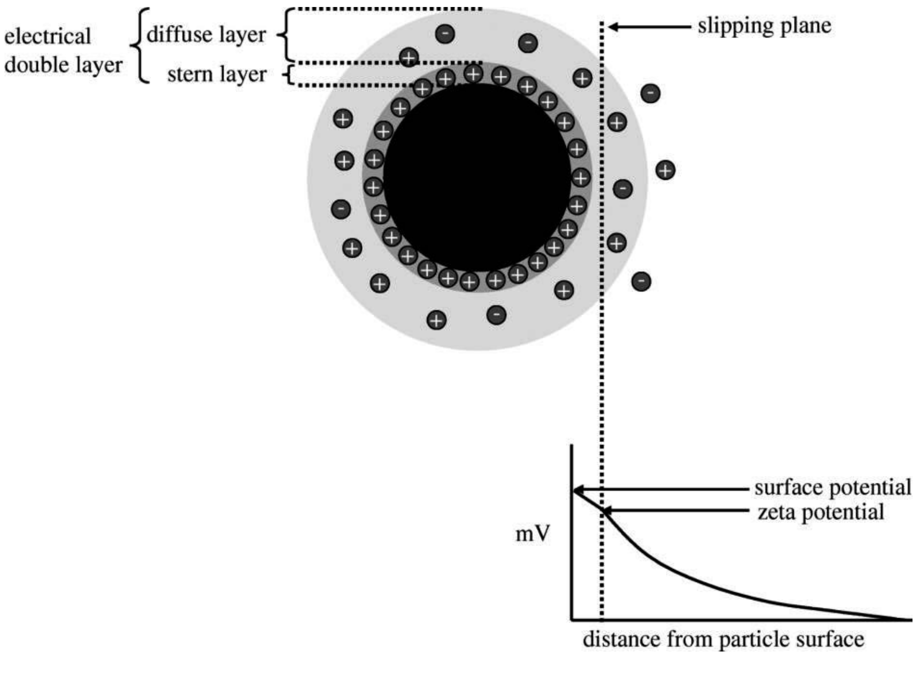

Figure 3. Diagram showing the electrical double layer that surrounds a particle in an aqueous medium and the position of the slipping plane (adapted from [21])

This double layer is formed when a surface-charge-carrying solid particle suspended in a liquid becomes surrounded by counter-ions of opposite charge to that of the particle surface. As the particle moves in the solution, the plane beyond which counter-ions do not migrate along with the particle is known as the slipping plane. The electrical potential at the slipping plane is the zeta potential and is typically measured in mV.

Although zeta potential is not equal to electric surface potential in the double layer, it is often used to characterize double-layer properties.[22]

The surface potential of a bilayer is a result of having charged ions adsorbed to it and the presence of glycoproteins, charged lipids or surfactants in the bilayer, such as didodecyldimethylammonium bromide (DDAB)[23] which is cationic (figure 4).

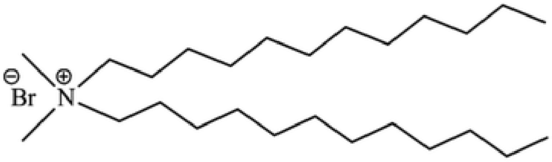

Figure 4. DDAB chemical structure

Due to its apolar interior, lipid bilayers are permeability barriers to diffusional equilibration of solutes between the two compartments it separates. Permeation of lipid bilayers by small polar molecules and ions seems to occur via one or a combination of both of two mechanisms depending on the nature of the permeants and the nature of the bilayers.[24] In a “solubility-diffusion” mechanism, the permeant partitions into the bilayer from one of the aqueous compartments, diffuses across it and leaves by dissolving into the second aqueous compartment. In a pore mechanism, the permeant diffuses through the bilayer via transient water-filled pores formed because of density fluctuations in it.[9]

1.3. Membrane fusion

Membrane fusion is involved in many cellular events, such as the release of neurotransmitters, invasion of enveloped viruses, intracellular trafficking of proteins and sperm-egg fertilization[25]. The complete fusion happens when the two membrane-bound entities merge into one and their contents are mixed together. In cells, fusion requires the action of lipids, proteins and fusion-triggering stimulants, which complicate the understanding of this complex fusion machinery.[26]

From model membrane studies it is known that the fusion process initiation demands the overcoming of several energy barriers. The first energy barrier is originated from the need to bring to close proximity the two membranes. After the aggregation of the membranes, there's a close apposition of the lipid bilayers. The next step is a destabilization transiently of the two membranes at the point of close approach, resulting in a bigger mixed membrane and both contents.[27]

Freeze and Thaw (FT) cycling is a technique often used in the preparation of liposomes. A common procedure is freezing the liposomes with liquid nitrogen and thawing at a temperature above the phase transition temperature of the lipids. In the preparation of liposomes, freeze-thaw cycling is implemented to reduce the lamellarity of liposomes, form a less polydispersed system and/or disrupt the liposomal bilayer to allow drug molecules to diffuse into the liposome, promoting encapsulation.[28] Disruption of the lipid-bilayer typically results in vesicle fusion, so this was used in mixtures of LUVs tagged with NBD, rhodamine or both, to obtain the efficiency of energy transfer (EET) of this process.

Monitoring lipid exchange or mixing and membrane fusion is commonly done using Förster Resonance Energy Transfer (FRET).[29] A classic donor-acceptor pair used for FRET measurements is NBD (7-nitro-2,1,3-benzoxadiazol-4-yl) and Lissamine rhodamine B sulfonyl.[30] When linked to a lipid, FRET measurements can be done to study lipid membranes. In this study we used NBD and rhodamine linked to 1,2-dipalmitoyl-*sn*-glycero-3-phosphoethanolamine (DPPE) (Figure 5) to label LUVs and GUVs, which can be visualized by fluorescence microscopy.

The figure 6 shows the overlapping of the emission spectra of NBD with the excitation of rhodamine.

Another way to study fusion is using LUVs that contain biotinylated lipids in their bilayer. The affinity of streptavidin for biotin is one of the strongest non-covalent biological interactions known, with a dissociation constant in the femtomolar range. Each streptavidin monomer can bind one biotin molecule, allowing a streptavidin protein to maximally bind four biotins (Figure 7).[31]

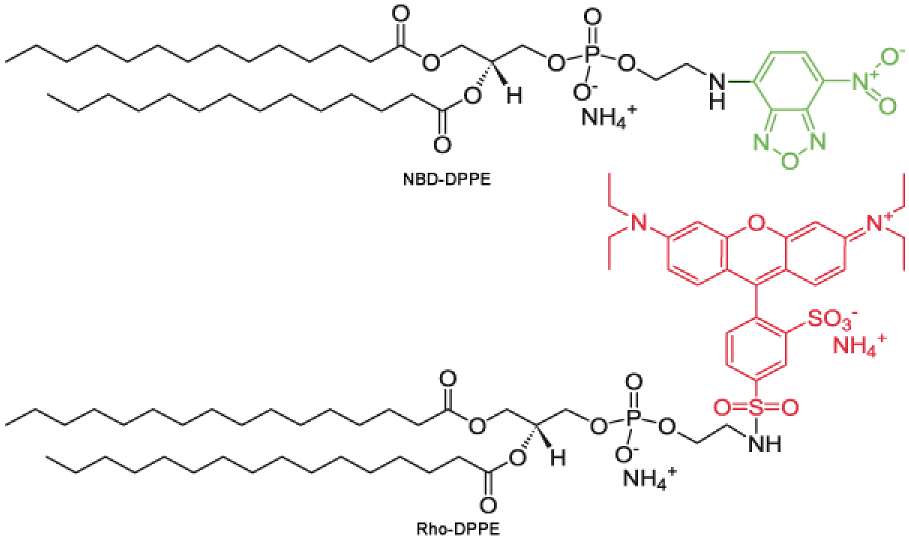

Figure 5. NBD-DPPE and Rho-DPPE chemical structures

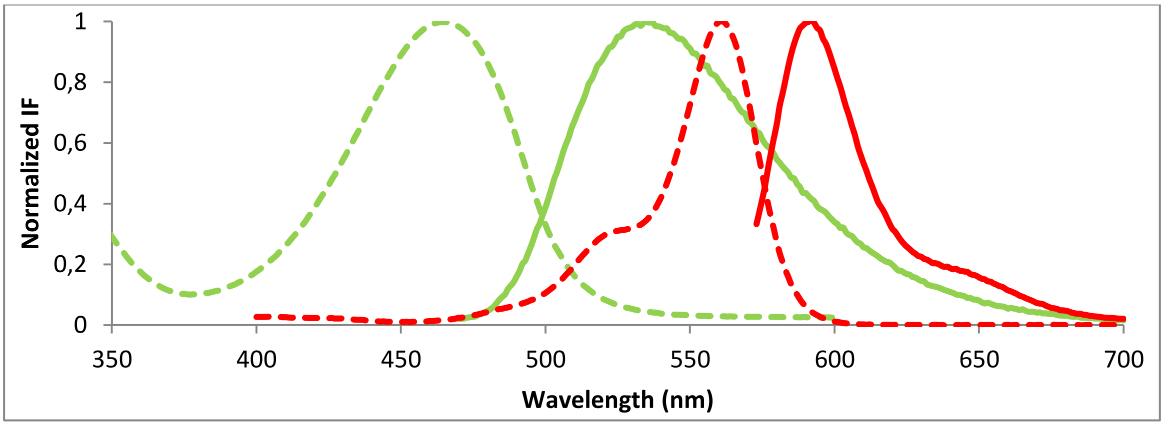

Figure 6. Normalized spectra of NBD (green) and Lissamine rhodamine B sulfonyl (red) (dashed line: excitation; full line: emission)

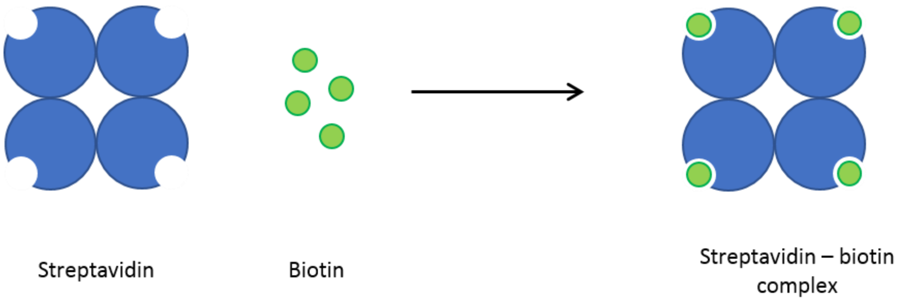

Figure 7. Biotin-Streptavidin binding
(adapted from https://www.expedeon.com/guides/antibody-labeling-guides/biotin-streptavid Q\11in-interaction/)

The biotinylated lipid used in this work is Biotin-X DHPE (N-((6-(Biotinoyl)amino)hexanoyl)-1,2-Dihexadecanoyl-sn-Glycero-3-Phosphoethanolamine, Triethylammonium Salt) (Figure 8).

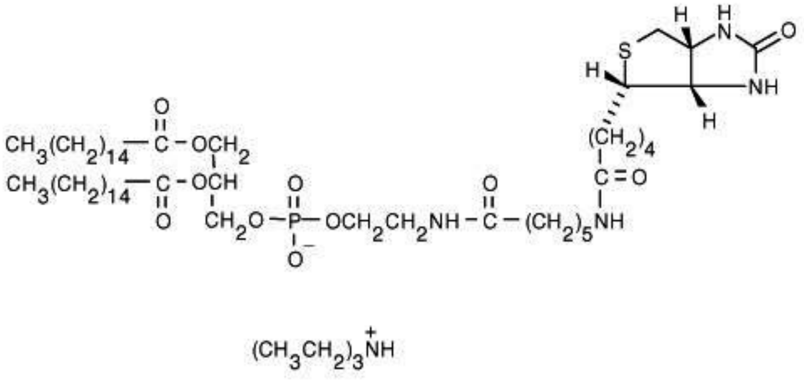

Figure 8. Biotin-X DHPE chemical structure

1.4. Membrane models

Due to biological membranes high complexity and in order to investigate the biological processes that occur on the surface or within the membrane lipid bilayer, numerous studies are performed using biomimetic model membranes (e.g. drug permeability[32,33] and drug and gene delivery[34,35]).

Liposomes are lipid vesicles that encapsulate a certain volume of aqueous media and are made by hydrating membrane lipids. Whereas lipid monolayers are constituted of only one lipid leaflet and therefore do not reflect the biological membranes structure complexity, lipid vesicles contain a bilayer, similarly to biological membranes.

Different types of vesicles can be obtained through different preparation methods (Figure 9).[7] Multilamellar lipid vesicles (MLV) are formed when a dried lipid film is hydrated and contain several concentric lipid bilayers separated by aqueous compartments. MLVs' size (0.5 - 10 µm) can be reduced and homogenized performing several freeze-thaw cycles and extrusion through a porous membrane, originating large unilamellar vesicles (LUV) (100 - 1000 nm).[36] Small unilamellar vesicles (SUV) (up to 100 nm) are obtained by sonicating

MLV.[37] Giant unilamellar vesicles (GUV) (bigger than 1 µm) can be obtained by hydrating a dried lipid film over a long period of time (gentle hydration method) or in presence of an external field (electroformation method).[3] Their size is comparable to that of eukaryotic cells, thus mimicking the same curvature and they can be viewed by fluorescence microscopy,[38] adding a fluorescently labeled lipid.

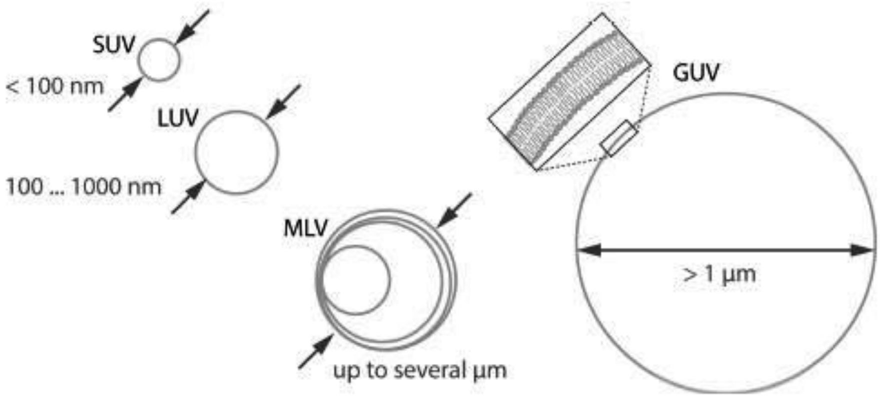

Figure 9. Lipid membranes model systems (adapted from [39])

In this work, GUVs formation was based on Weinberger et al. (2013) procedure by polymer-assisted swelling (Figure 10).[3] Aside from its simplicity (for details see Materials and Methods section), the main advantage of this method is that the swollen vesicles do not contain any remnants of the polymer inside since the lipids do not penetrate the PVA film, but rather assemble on top of the matrix to several stacks of lipid bilayers. Furthermore, PVA does not dissolve in solution at room temperature and thus there is no detectable PVA impurity in the membrane.[39]

MLVs are generally not used due to the complexity of having many internal volumes, which makes interpretation difficult.[7] For this reason, unilamellar vesicles such as LUVs and GUVs were chosen instead.

LUVs advantages rely on the homogeneity of produced LUVs, versatility of the lipid bilayer composition and the average bilayer curvature being practically the same as planar membranes. GUVs size and curvature is the most similar to cells and easily seen via microscopy techniques, however their fragility is bigger as they do not contain a cytoskeleton.

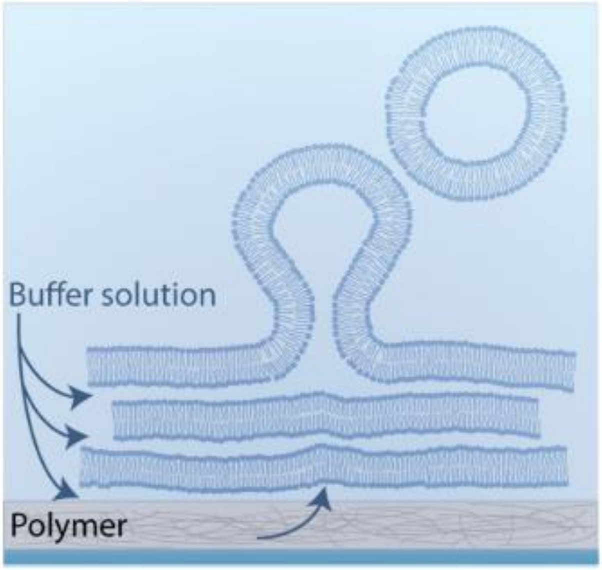

Figure 10. Schematic illustration of polymer-assisted swelling: upon hydration of a dried lipid film, vesicles swell from below
(adapted from [39])

Liposomes offer several advantages including biocompatibility, capacity for self-assembly, ability to carry large drug quantities, and a wide range of physicochemical and biophysical properties that can be modified to control their biological characteristics.

Clinical uses for liposomes are underway, e.g. liposomes containing drugs or DNA can be injected into patients. These liposomes fuse with the plasma membrane of many kinds of cells, introducing their content into them.[5,40]

1.5. Permeability of biological membranes

A primary goal in drug delivery research and drug development in general is to identify delivery systems that increase drug efficacy at an intended action site while reducing toxicity to healthy tissues or resorting to invasive techniques. The ability of a drug to permeate cell membranes can be enhanced manipulating membranes permeation through chemical modification, administration route, dosage or delivery system design.

Mechanisms for molecular transport across membranes can be divided by physical principle into two categories: active and passive transport. While the former requires regulatory machinery, with input of energy, that transports the target molecules in the direction opposed to the concentration gradient, the latter proceeds via an entropy-driven, nonspecific diffusion process of the molecule across the membrane. Most of small neutral molecules and drug molecules are transported passively through the membrane.

According to Lipinski et al., the rule-of-five predicts suitable drug candidates for body intake (primarily aimed for oral delivery) based on solubility and diffusion of drugs across biological barriers, which results in the following postulates: octanol/water partition coefficient logarithm ≤ 5, molecular weight under 500 D and not more than 5 hydrogen bonds donors, not more than 10 hydrogen bond acceptors.[41] However these drugs can easily be eliminated and because of that, transdermal drug delivery techniques have been studied as a non-invasive alternative that avoids liver first-pass metabolism and prevents the exposure to chemical and biological conditions of the gastrointestinal tract.

Carboxyfluorescein (CBF) (figure 11.A) is a fluorescent probe used in several pharmaceutical and biochemical applications.[42] Due to its carboxylic and hydroxyl groups, this drug is highly dependent of the pH. CBF release from LUVs was proved to have a prolonged kinetic profile, so, adding a monosaccharide chain to this molecule would only slow even more the permeation due to the higher molecular weight, while also being more difficult to obtain one CBF linked to only one chain due to having two carboxylic groups to which the linkage would occur. To avoid this, Fluorescein (which has one less carboxylic group than CBF) (Figure 11.B) was encapsulated in LUVs at a higher pH than physiological, to slow the permeation.

Since it has only one carboxylic group, synthesis of a fluorescein derivative with an amine group linked to the carboxylic group was tested so that the new molecule would be linked to increasingly higher number of monosaccharide chains, and this homologous series of molecules would, in suite, be encapsulated in liposomes for permeability studies. Such process requires a lot of time, so, for this thesis, one derivative of fluorescein was chosen to pursue the experiments.

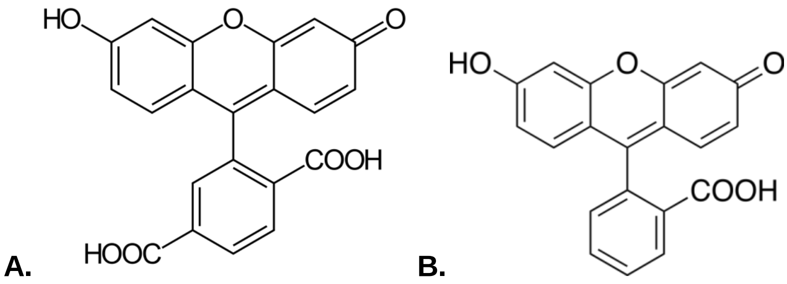

Figure 11. Chemical structures of CBF (A) and fluorescein (B)

Fluorescein Isothiocyanate-dextran (FITC-dextran) (Figure 12) is a fluorescent probe used extensively in cell permeability studies. Due to its high molecular weight and size, this molecule was chosen as a model for a better understanding of the mechanism of permeability of big molecules, like DNA, through the lipid bilayer.

Liposomes have been studied extensively for drug delivery purposes. The permeability of the phospholipid bilayer membranes of liposomes is influenced by factors such as lipid composition, temperature, and the presence of chemicals in the medium in which they are dispersed (e.g. pH of the solution).[43]

Besides these factors, the permeabilization of biological barriers can also be affected by other means, such as the use of lasers to generate acoustic waves.[44–47]

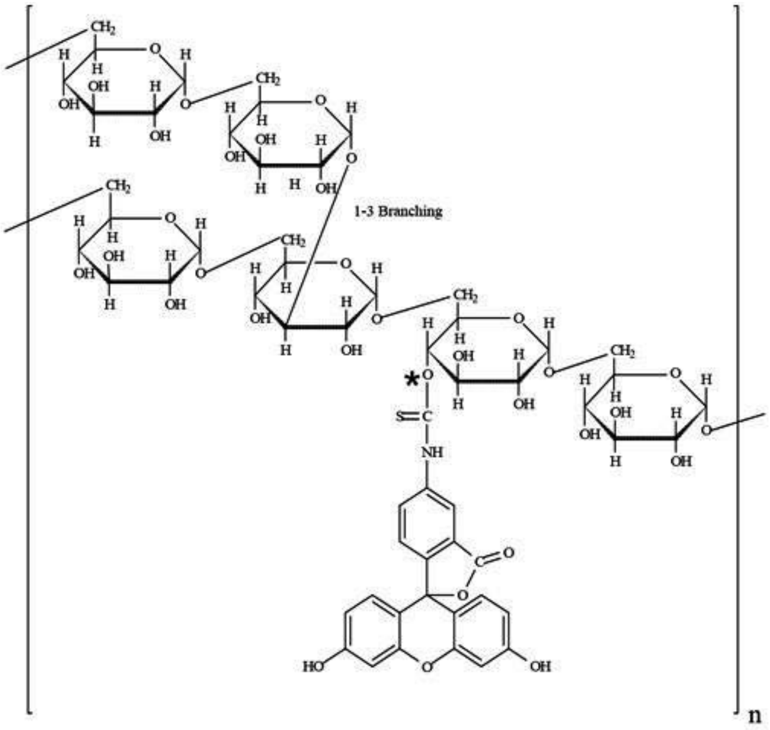

* The site of attachment of FITC is assumed to be randomly associated with any free hydroxyl group

Figure 12. FITC-dextran chemical structure (adapted from https://www.sigmaaldrich.com/content/dam/sigma-aldrich/articles/protocols/biology/fluorescein-image.jpg)

1.6. Photoacoustic waves

Lasers produce high optical energies over a small area generating stress waves due to the absorption of light by material with efficient light-to-pressure conversion.

Two types of stress waves can be produced by laser irradiation. Shock waves by dielectric breakdown and material ablation are characterized by a sudden discontinuous change in the material properties (melting) that propagates at supersonic speed, inducing an enormous rise in the pressure and temperature of the traversed medium.[48] Photoacoustic waves are due to thermoelastic expansion that involves the transient heating of the material surface, which propagates into the material at the speed of sound, with a moderate rise in the system pressure.

Acoustic methods also include the acoustic waves of therapeutic or diagnostic ultrasound (US) with high frequencies (MHz), which are characterized by compressional and rarefactional peaks of comparable amplitudes. When such acoustic waves propagate in liquids or tissues, they induce cavitation which, for critical acoustic energies, implode and produce shock waves.

Recently gene transfection mediated by laser light has received considerable attention due to notable advantages such as control of laser energy and possibility of introduction into the clinical practice.

Mechanisms by which laser irradiation and laser-generated stress transients perturb cell membranes are still under investigation.[49,50] High frequencies and high maximum pressure of PA waves lead to high stress gradients and high impulses that enable less common mechanisms of interaction between US and cells. GHz frequency acoustic waves have been shown to interact with cell membranes and contribute to membrane deformation.[51,52]

So, allying the previous information to the fact that liposomes can deliver a myriad of molecules ranging from drugs, to proteins or DNA, the aim of this study involves studying the effect of PA waves on lipid vesicles.

An acoustic wave is a mechanical wave that results from the back and forth vibration of the medium particles through which the wave is traversing. The particles motion is parallel or anti-parallel to the direction of the energy transport. The longitudinal wave consists of a repeating pattern of compressions and rarefactions, respectively, high pressure and low-pressure regions moving through a medium, i.e. a pressure wave (Figure 13).

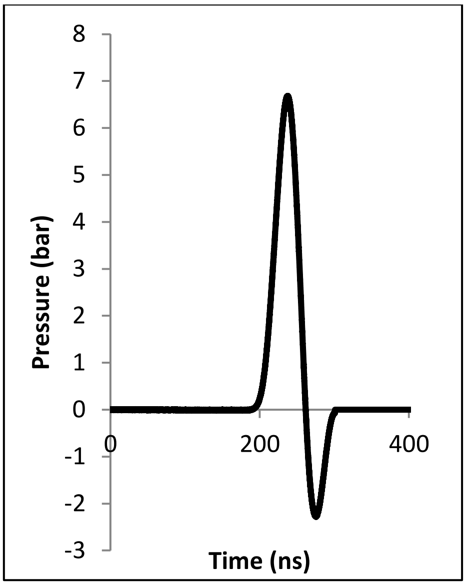

Figure 13. Typical pressure wave produced as a result of absorption of a 100 mJ/cm^2 energy at 532 nm by a piezophotonic film and mirror (0.6 mm), obtained with a needle hydrophone

The acoustic wavelength of the produced wave depends on the frequency of the pressure wave, but also the propagation rate of the medium in which it propagates.

Chapter 2:

Materials and Methods

2.1. LUVs preparation

The lipid mixtures containing the appropriate amounts of each lipid dissolved in chloroform were mixed in a vortex. The solvent was evaporated to total dryness under a stream of nitrogen while the solution was heated by blowing hot air on the tube. The lipid film was left under vacuum for 1h and maintained in the vacuum desiccator for around 12h to remove any trace amounts of solvent. The dry lipid was hydrated with an aqueous solution in a water bath heated to 40ºC. The tubes were then submitted to vortex cycles until the lipid film was entirely hydrated and then transferred to plastic tubes (Falcon). The resulting MLV suspensions were extruded through two stacked polycarbonate filters (Whatman Nucleopore) using a water-jacketed extruder (Lipex Biomembranes, Inc., Vancouver, Canada) at 40ºC. The lipid mixtures were subjected to 3 cycles of Freeze and Thaw, cooling to -196ºC with liquid nitrogen and heating up to 40ºC in a water bath, each followed with a vortex cycle and an extrusion. This procedure was adapted from Hope et al. (1985)[36]. After that, 10 extrusions and vortex cycles were performed. All the LUV samples were used within 1-2 weeks and were stored at 4-8ºC and protected from light exposure. POPC, POPS, POPE, NBD-DPPE and Rho-DPPE are from Avanti Polar Lipids, Biotin-X DHPE from ThermoFisher and DDAB from Aldrich.

2.2. Characterization of liposomes

Liposome size and polydispersity index (PDI) were determined by dynamic light scattering (DLS) using a Nanosizer ZS (Malvern Instruments). Data was collected at 25ºC and scattering angle 173º. The zeta potential of the liposomes was determined by laser Doppler velocimetry using a Nanosizer ZS with a disposable folded capillary cell with a 12.8º scattering angle.

2.3. Efficiency of Energy Transfer (EET)

To obtain the EET, two methodologies were adopted: Freeze and Thaw cycles (to mix LUV-NBD with LUV-Rho to obtain LUVs with both probes) via steady state fluorescence measurements; and by adding different percentages of LUVs labeled with both probes to a mixture of LUV-NBD and LUV-Rho, via both steady state and time-resolved fluorescence measurements.

The presence of increasing concentrations of vesicles containing both donor (NBD) and acceptor (Rho) was obtained by repeated FT cycles on LUVs mixtures of different proportions of LUVs containing only the donor or only the acceptor. When the aqueous media contained saccharides (glucose or sucrose), FT cycles were not efficient regarding fusion/fission of the LUVs. In this case, increasing fractions of LUVs prepared with both donor and acceptor were used.

Steady state fluorescence emission spectra were collected after excitation at the maximum absorption of the probes (450 and 568 nm, for NBD and Rho, respectively). Excitation spectra were obtained collecting fluorescence at the emission maxima (530 and 590 nm, of NBD and Rho, respectively).

All of the LUVs in this section were obtained by extrusion through 2 polycarbonate filters with pore size of 400 nm.

First, fluorescence measurements of Freeze and Thaw were tested on LUVs only constituted of POPC and hydrated with glucose 280mM. As FT was not successful in these LUVs due to the aqueous media containing cryoprotectant glucose, new LUVs were prepared with different compositions (Table 2) and were hydrated with water.

The stability of the mixture of LUV-NBD and LUV-Rho (LUV-mix) in equal proportions was evaluated every hour. To study the effect of FT, 20µL of the LUV-mix were taken as control and diluted with 980µL of water. Then, one cycle of FT was performed on the remaining mixture and 20µL were taken out and diluted, obtaining FT1. The following FT2 and FT3 were obtained after a second and third cycle of freeze and thaw, respectively.

Table 2. Lipid composition (%) of LUVs negatively charged (with NBD and POPS, named LUV-NBD), LUVs positively charged (containing rhodamine and DDAB, named LUV-Rho) and LUVs with both charges and probes (LUV-NBD-Rho)

Sample	POPC	POPE	POPS	DDAB	NBD-DPPE	Rho-DPPE
LUV-Rho	74	20	0	5	0	1
LUV-NBD	74	20	5	0	1	0
LUV-NBD-Rho	74	20	2.5	2.5	0.5	0.5

For the study of the effect of FT on different LUV mixtures where donor and acceptor mol% varied (Table 3), essays were performed before and after FT, taking 20 µL of the sample and diluting with 980 µL of water, and then 20 µL of the mixture after FT and dilute it.

Table 3. LUVs mixtures of LUVs from Table 2 for the study of the EET varying the acceptor fraction

Sample	LUV-Rho	LUV-NBD	LUV-NBD-Rho	H_2O
1	50	0	0	50
2	45	5	0	50
3	40	10	0	50
4	35	15	0	50
5	30	20	0	50
6	25	25	0	50
7	20	30	0	50
8	15	35	0	50
9	10	40	0	50
10	5	45	0	50
11	0	50	0	50
12	0	0	50	50

Time-resolved fluorescence emission was obtained for LUV-NBD (100% of donor), LUV-NBD-Rho (50% of donor and 50% of acceptor), and several mixtures of LUV-NBD and LUV-Rho in the same proportion with LUV-NBD-Rho percentages (0 to 50%). This was done using charged LUVs (LUVs AD, table 4), and biotinylated LUVs (LUVs BS, table 5).

Table 4. Lipid composition (%) of LUVs AD (LUV-NBD, LUV-Rho and LUV-NBD-Rho)

LUVs AD	POPC	POPE	POPS	DDAB	NBD-DPPE	Rho-DPPE	LPPC
LUV-NBD	73	20	5	0	1	0	1
LUV-Rho	73	20	0	5	0	1	1
LUV-NBD-Rho	73	20	2.5	2.5	0.5	0.5	1

Table 5. Lipid composition (mM) of LUVs BS (LUV-NBD, LUV-Rho, LUV-NBD-Rho)

LUVs BS	POPC	Biotin	NBD-DPPE	Rho-DPPE
LUV-NBD	20	0.2	0.2	0
LUV-Rho	20	0.2	0	0.2
LUV-NBD-Rho	20	0.2	0.1	0.1

Table 6. Samples composition (%) using LUVs AD (D, contains only LUV-NBD; AD, contains only LUV-NBD-Rho; AD0 to AD50, contain LUV-NBD, LUV-Rho and LUV-NBD-Rho)

Sample	LUV-NBD	LUV-Rho	LUV-NBD-Rho
D	100	0	0
AD	0	0	100
AD0	50	50	0
AD10	45	45	10
AD20	40	40	20
AD30	35	35	30
AD40	30	30	40
AD50	25	25	50

Table 7. Samples composition (%) using LUVs BS (ABD, contains only LUV-NBD; ABAD, contains only LUV-NBD-Rho; ABAD0 to ABAD50, contain LUV-NBD, LUV-Rho and LUV-NBD-Rho)

Sample	LUV-NBD	LUV-Rho	LUV-NBD-Rho
ABD	100	0	0
ABAD	0	0	100
ABAD0	50	50	0
ABAD10	45	45	10
ABAD20	40	40	20
ABAD30	35	35	30
ABAD40	30	30	40
ABAD50	25	25	50

LUVs AD were hydrated and diluted with an aqueous sucrose solution (280 mM) and LUVs BS were hydrated with an aqueous sucrose solution (280 mOsm) to mimic the GUVs conditions.

Several samples with different compositions (Tables 6 and 7) were prepared for the FRET studies. Samples of LUVs AD were obtained by diluting 20µL in total of LUVs in 480µL of sucrose. LUVs BS samples were prepared by diluting 40µL of the LUVs mixture with 40µL of Streptavidin and 420 µL of sucrose. Streptavidin (0.2 mg/mL) was prepared solubilizing the protein with a PBS solution (280 mOsm made with NaCl 0.13 M, Na_2HPO_4 10mM and NaH_2PO_4 10mM).

2.4. Fluorescein permeability

Steady state fluorescence spectra and release kinetics measurements were performed on a Cary Eclipse fluorescence spectrophotometer (Varian) equipped with a thermostatted multicell holder accessory.

LUVs in these permeability essays were only composed of POPC. The film was hydrated with a PBS solution A (Na_2HPO_4 50 mM, NaCl 100 mM both from Sigma, ethylenediaminetetraacetic acid (EDTA) 1 mM from General Purpose Reagents and NaN_3 0.02% from Fluka) containing Fluorescein 10 mM (Sigma) and adjusted to pH = 8 and were extruded with filters of 100 nm pore size.

After the extrusion, LUVs passed through 3 Sephadex G-25 exclusion columns (HiTrap Desalting from GE Healthcare) of 5 mL (25mm of height) in series, previously equilibrated with PBS solution B (without fluorescein and 10mM more NaCl), adjusted at pH = 8, too. The sample was eluted with PBS solution B and the first fractions collected into glass tubes. With this chromatographic technique, smaller molecules (uncapsulated dye) are trapped inside the beads of the stationary phase while bigger molecules (LUVs) pass through the spaces between the beads, arriving first at the end of the column. The fractions containing the LUVs (1 to 1.5 ml) were diluted with PBS solution B to a final lipid concentration of 0.1 mM. The same experiment was repeated using PBS solutions with pH = 9.

The kinetics of fluorescein permeation through the POPC bilayer was followed by fluorescence (excitation at the absorption maximum, 492 nm, and collection at the emission maximum, 517 nm), at both 25 and 35°C. At the high concentration of fluorescein in the aqueous compartment inside the LUVs, the fluorescence is small due to fluorescein self-quenching.[55] After permeating through the lipid bilayer into the aqueous compartment outside the LUVs, fluorescein is diluted by several orders of magnitude and its fluorescence intensity increases.

The maximum of fluorescence (corresponding to 100% permeation) was obtained by adding 100 µL of a 10% Triton X-100 (TX) solution to the cuvettes containing the LUVs suspensions. TX is a nonionic surfactant and when added to liposomes, it destroys their membrane causing the release of fluorescein and consequently an increase in fluorescence intensity to its maximum.[56]

2.5. Synthesis of the Fluorescein derivative

The objective was to prepare fluorescein derivatives after reaction with ethanolamine and saccharides of increased molecular weight (mono-, di- and oligosaccharides). This was attempted through the acetylation of the saccharide moiety followed by reaction with fluorescein-ETA that also had to be synthesized.

Glucose acetylation was done by following Silva et al. (2013) protocol.[53] A 25 mL round flask was charged with D-glucose (5.0 g, 27.8 mmol), acetic anhydride (25 mL) and 3.5 mol% I_2 (0.25 g, 1 mmol) in one portion. The reaction mixture was irradiated in a ultrasonic water bath at ambient temperature for 20 min. The resulting mixture was washed with 20% sodium thiosulfate ($Na_2S_2O_3$) and extracted with dichloromethane. The combined organic layers were washed with saturated sodium bicarbonate ($NaHCO_3$) (30 mL). After drying over anhydrous sodium sulfate (Na_2SO_4), the solvent was removed under vacuum. The peracetylated D-glucose **1.1** was obtained as a colorless solid.

The fluorescein derivative synthesis was adapted from Xu et al. (2012) protocol[54]. In a 25 mL round flask, 0.2 mmol (0.066 g) of fluorescein, 0.22 mmol of N-(3-Dimethylaminopropyl)-N'-ethylcarbodiimide hydrochloride (EDC) (0.034 g) and 0.2 mmol NEt$_3$ (28 µL) were added to 20 mL of ethyl acetate at room temperature. After magnetic stirring for 2h, ethanolamine (ETA) in excess (1 mL) was added and the solution was left to react during 24h. Acetic acid was added to precipitate the product **2.1** and thin layer chromatography (TLC) was performed. Several modifications of this new protocol (**2**) were done: adding 0.22 mmol of hydroxybenzotriazole (HOBT) (0.034 g) to the EDC and fluorescein mixture before adding NEt$_3$, obtaining product **2.2**; same conditions as previous but using 10 mL of water as solvent instead of ethyl acetate, **2.3** is obtained; same conditions as previous but reaction was performed on a bath at 80ºC, product formed is **2.4**; same conditions as the protocol (**2**) but using 20 mL of Phosphate Saline Buffer (PBS) (containing NaCl 150mM and Na$_2$HPO$_4$ 10mM, adjusted at pH=6) as solvent and adding 10 mL of methanol after adding the ethanolamine, obtaining **2.5**. Another synthetic route was tested, fluorescein (10 mg), DCC (50 mg), HOBT (45 mg) and ETA (30µL) were all mixed and submitted to mechanical force, using a press setup developed by Marta Piñeiro (under development, used at the Department of Mechanical Engineering of the University of Coimbra), obtaining product **2.6**. Products **2.1** to **2.4** were characterized by NMR, **2.5** and **2.6** by HPLC.

2.6. GUVs preparation by PVA-assisted swelling

Giant Unilamelar Vesicles (GUVs) were prepared by a gel-assisted swelling method, according to the published protocol from Weinberger et al. (2013)[3]. A solution of 5% (w/w) polyvinyl alcohol (PVA) was prepared mixing PVA (145 kD) and an aqueous solution 280mM sucrose, stirring on a heat plate at 90ºC until the solution was clear. On an uncoated µ-slide 8 well (Ibidi, Germany) PVA was spincoated on each well, 150µL of the PVA solution using a spincoater (Speciality Coating Systems, Inc., Model P6700) with the program in Table 8.

Table 8. Spincoating rpm program

Time (s)	rpm	
	initial	final

1	0	400
10	400	400
5	400	2500
60	2500	2500
1	2500	0

The coated slide was placed for 2h in an oven at 37°C and afterwards kept inside a closed desiccator until the lipid application. Rho-DPPE and NBD-DPPE were added to POPC in a 1:100 ratio, to later prepare GUV-Rho and GUV-NBD, respectively. The lipid mixtures used were stocked in chloroform to a final concentration of 1.5 mM. 10µL of each lipid solution were deposited uniformly per well over the dry PVA film, placing the slide on a moderately hot plate to assure the solvent evaporates faster and doesn’t compromise the film. The lipid coated slide was then put under vacuum for 15 minutes. 300µL of a 280mM aqueous solution of sucrose or a FITC-dextran (Sigma-Aldrich, 4kD) aqueous sucrose solution (measured pH = 7.1) were added onto each well to hydrate the PVA film. The slides were kept in the dark for 2h to allow the formation of GUVs. After the formation, the solutions containing the GUVs were gently removed to avoid contaminations with PVA, placed in Eppendorfs and stored in the dark before use. The formed vesicles were then suspended in a glucose solution with the same saccharide concentration (280 mM) to obtain isotonic conditions. Due to glucose’s lower molecular weight, this solution’s density is lower than sucrose, which induces GUVs sedimentation.

2.7. GUVs imaging

A confocal fluorescence microscope (Carl Zeiss) at the MICC Imaging Facility of CNC (Centre for Neuroscience and Cell Biology, Coimbra) and an inverted microscope (Olympus CKX41SF-5) coupled to a fluorescence system (Olympus URFLT50) at the CQC (Coimbra Chemistry Center) were used for image acquisition of GUVs. The transmission of blue and green excitation filters is shown in figure 14.

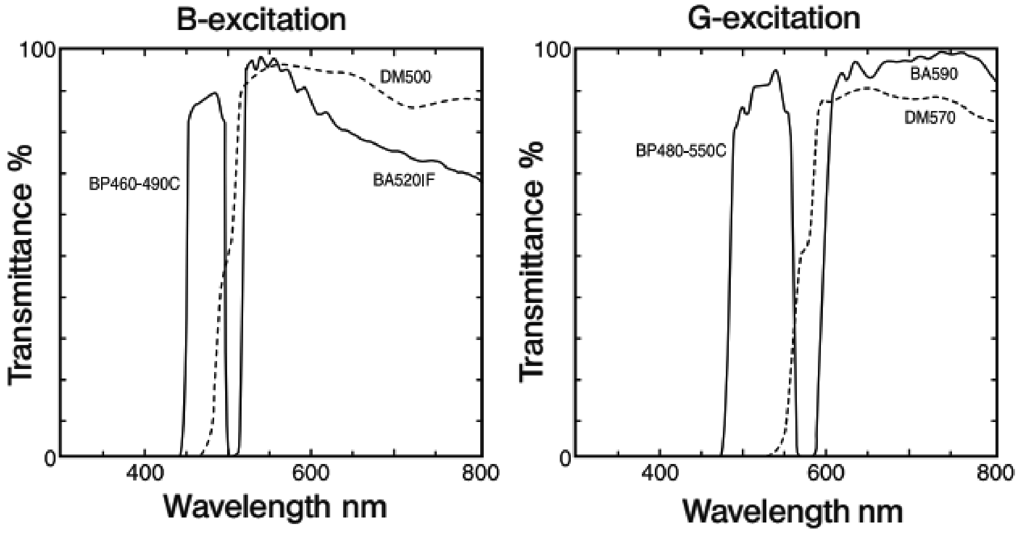

Figure 14. NBD and FITC-dextran were detected using the excitation filter BP460-490 nm (blue light source) and rhodamine with the BP480-550 nm (green light source)

(Adapted from http://cn.olympus.com/upload/accessory/20114/201141112595675 6088.pdf)

For microscopy observation, GUVs were diluted 5 times (1:5 dilution) with an aqueous glucose solution (280 mM).

For GUVs hydrated with FITC-dextran several dilutions with glucose solution were performed to obtain the best contrast between the inside and the outside media, when viewing using the green channel.

To obtain more homogenous samples (with less smaller GUVs) after dilution of GUVs with FITC-dextran, two procedures were tested: centrifugation using a UEC Micro 14/B centrifuge at 10500 rpm (8998 *G*) during 10s, 30s, 1 minute and 5 minutes; and just by earth's gravitational force and waiting 45 minutes for GUVs to deposit at the bottom of the tube, collecting only the "pellet" of the sample for later use.

2.8. Photoacoustic waves application

Light-to-pressure transducer films were kindly provided by LaserLeap Technologies, S.A. (Coimbra, Portugal). The photoacoustic (PA) waves application was performed using an adapted set-up (Figure 15) originally developed by Serpa et al. (2008).[57] The samples of LUVs were irradiated through a quartz window with a Spectra Physics Quanta Ray GCR-130 laser of 532nm with pulses of 8 nanoseconds.

For the PA waves application, a mixture of LUV-NBD and LUV-Rho of LUVs AD (table 5) (1:1) and a mixture of LUV-NBD and LUV-Rho of LUVs BS (table 6) and Streptavidin (1:1:2) were used. 150µL of the mixture were dropped on the mirror surface of the setup and PA waves were applied for 10 and 20 minutes using 100 and 200 mJ/cm^2 fluencies. After the laser application, for LUVs AD 20µL of the sample were collected and diluted with 480µL of sucrose and for LUVs BS 10µL were diluted in 490µL of sucrose. These final diluted samples were then used for fluorescence studies to evaluate the EET.

Another method of application of the LUVs on the setup consisted in dropping 50µL of the mixture onto the mirror surface and trapping the drop with a cover glass (Marienfeld, Germany), figure 15 (left). This set-up was built to avoid the possible evaporation of the solvent from the GUVs suspension that could happen at higher laser fluencies.

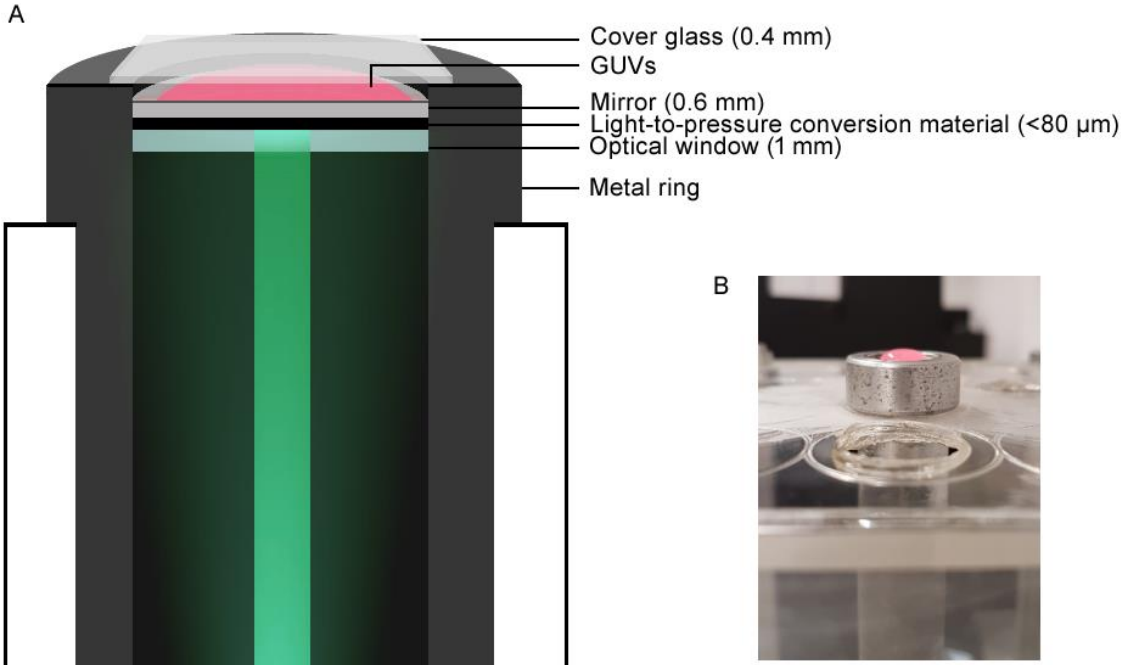

Figure 15. A. Illustration of setup used for PA waves application (not in scale); B. Photography of setup

The PA waves thermoelastic expansion is, in principle, non-destructive, however in practice, signs of material fatigue are apparent after thousands of shots. As this is visually characterized by a change in color and a decrease in opacity of the films, the films used in the experiments were regularly replaced. The laser pulse energy was measured with a Power Meter (Newport Model 1918-C) and has a diameter of 3 mm corresponding to 0.07 cm^2 of area. Different exposure times to the PA waves (10 and 20 minutes) and fluencies (40, 100, 200 and 400 mJ/cm^2), at a 10 Hz repetition rate.[58]

2.9. Techniques

2.9.1. Dynamic Light Scattering (DLS)

Light scattering is a consequence of the interaction of light with the electric field of a small particle or molecule. An incident photon induces an oscillating dipole in the electron cloud. As the dipole changes, energy is radiated in all directions. This radiated energy is called “scattered light”.[59]

Mie theory is an exact description of how spherical particles of all sizes and optical properties scatter light.[60]

Dynamic light scattering is a non-invasive technique for measuring the size of particles and molecules in suspension. Brownian motion is the random movement of particles due to collisions caused by bombardment by the solvent molecules that surround them. The technique of DLS measures the speed of particles undergoing Brownian motion.

The polidispersity index (PDI) is a dimensionless measure of the broadness of the size distribution calculated from the cumulants analysis. Between 0.08 to 0.7 (mid-range value of PDI) the distribution algorithms operate the best. These values were provided by Malvern Instruments user guide.

2.9.2. Zeta potential

Electrophoresis is the movement of a charged particle relative to the liquid it is suspended in under the influence of an applied electric field. Particles move with a velocity which is dependent on: Zeta potential, field strength, dielectric constant of medium and viscosity of the medium.[59]

By measuring Electrophoresis using the Doppler Effect, in which a laser beam is passed through a sample undergoing electrophoresis and the scattered light from the moving particles is frequency shifted, we obtain the zeta potential as the difference between the reference frequency and the scattered beam frequency.

2.9.3. Time-Correlated Single Photon Counting (TCSPC)

Fluorescence based techniques such as steady state fluorescence and Förster Resonance Energy Transfer (FRET), allow quantitative measurements of membrane dynamics (e.g. membrane fusion, distance between fluorophores, association of macromolecules, fluorescence anisotropy).[61,62] When radiation falls on a chromophore, the excited molecule can return to its fundamental state by emission of energy. Light energy is absorbed by a chromophore on a 10^{-15} s time scale; the energy can be re-emitted by fluorescence on a 10^{-9} s time scale. However, other possibilities are that the excited molecule can transfer its energy without radiation to another fluorophore which in turn fluoresces in the same order of time. This latter phenomenon is called FRET. The events taking place can be analyzed using a Jablonski diagram (Figure 16).

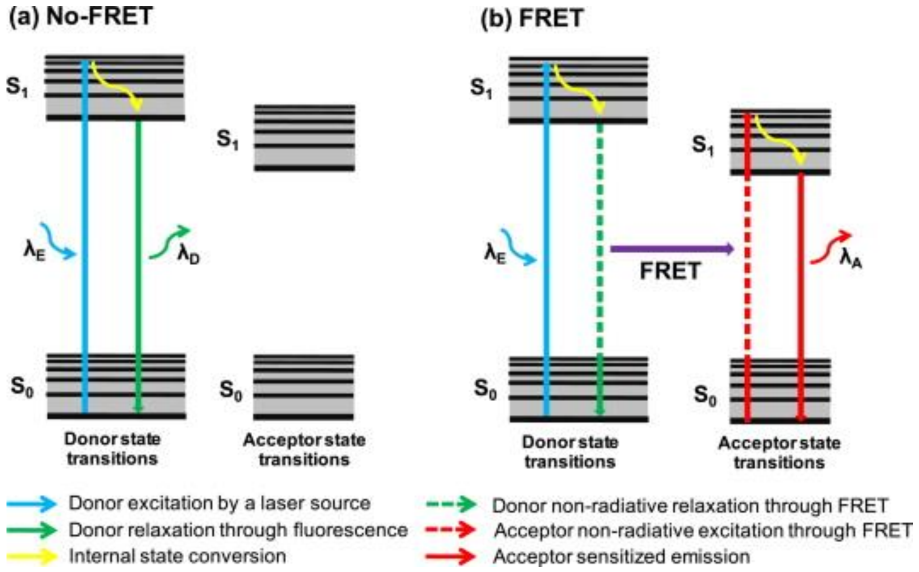

Figure 16. Jablonski diagram for the case of (a) fluorescence (no FRET) and (b) when FRET is the only possible quenching mechanism

(adapted from [63])

In FRET, an initially electronically excited fluorophore (donor, *D*) transfers its excitation energy in a non-radiative way through long-range dipole-dipole interactions, to another chromophore (acceptor, *A*) and the latter, which is initially in electronic ground state, becomes excited and may or not fluoresce.[64] FRET doesn't involve photon emission or molecular contact between the two species, but is highly dependent on the distance between them. Quenching of the donor excited state (whose lifetime in absence of acceptor is τ_D) by FRET to an acceptor located at a relative distance, *r*, follows first order kinetics and the rate constant is proportional to the inverse sixth power of this distance, given by

$$k = \frac{1}{\tau_D}\left(\frac{R_0}{r}\right)^6 \tag{1}$$

where R_0 is the Förster distance of donor-acceptor pair, i.e. the distance at which the energy transfer efficiency is 50% (values lie in the 10–60 A range for typical *DA* FRET pairs).[65]

For non-identical donor and acceptor, the FRET efficiency or efficiency of energy transfer (EET) can be quantified from the reduction in donor quantum yield (or fluorescence intensity, IF) or lifetime in the presence of acceptor (donor-acceptor, *DA*)[66], by (2)

$$EET = 1 - \frac{\tau_{DA}}{\tau_D} = 1 - \frac{IF_{DA}}{IF_D} \tag{2}$$

For FRET to occur there are a few criteria that need to be met, namely the fluorescence emission spectrum of the donor molecule must overlap the excitation spectrum of the acceptor chromophore and the two species must be in the close proximity to one another (typically 1 - 10 nm).[66] EET depends on the donor-to-acceptor separation distance *r*, and the Förster distance of this pair R_0, expressed by

$$EET = \frac{1}{1+\left(\frac{r}{R_0}\right)^6} \tag{3}$$

The Förster distance, i.e. the distance at which the energy transfer efficiency is 50%,[67] depends on the overlap integral of donor emission spectrum with the acceptor absorption spectrum and their molecular orientation, as expressed by the following equation

$$R_0{}^6 = \frac{2.07}{128\pi^5 N_A}\frac{k^2 Q_D}{n^4}\int F_D(\lambda)\epsilon_A(\lambda)\lambda^4 d\lambda \tag{4}$$

where Q_D is the fluorescence quantum yield of the donor in the absence of acceptor, k^2 is the dipole orientation factor, *n* is the refractive index of the medium, N_A is the Avogadro number, F_D is the normalized donor fluorescence and ϵ_A the acceptor extinction coefficient.

Time-Correlated Single Photon Counting (TCSPC) is used to determine the fluorescence lifetime and consequently the amount of FRET, measuring the time between sample excitation by a pulsed laser and the arrival of the emitted photon at the detector. TCSPC requires a defined “start”, provided by the electronics steering the laser pulse or a photodiode, and a defined “stop” signal, realized by detection with single-photon sensitive detectors. The measurement of this time delay is repeated many times in a stochastic process to account for the statistical nature of the fluorophores emission and the delay times are sorted into a histogram that plots the occurrence of emission over time after the excitation pulse. Most photons reach the detector soon after the excitation pulse followed by a drastic decrease of the number of photons with time. Fluorescence lifetime is determined by fitting this histogram with an exponential decaying function.[68]

Time-resolved fluorescence decays were performed using a home-built picosecond Time-Correlated Single Photon Counting (TCSPC) apparatus, described in detail by Pina et al. (2009)[69]. A picoQuant picoled model LDH-P-C-450B with λ_{exc} = 451nm was used as excitation source. Fluorescence decays and the instrumental response function were collected in a time scale corresponding to 1024 channels in a 48.8 ps/channel, until the maximum of 3000 counts were reached. Deconvolution of the fluorescence decay curves was performed using modulation function method, as implemented by G. Striker in the SAND program, as reported in the literature.[70]

Data resulting from the global analysis of the decays were fitted with sums of two exponentials (for LUV-NBD) and three exponentials (for LUV-NBD-Rho and the LUVs mixtures),

$$I_{LUV}(t) = \sum_{i=1}^{n} a_i e^{-t/\tau_i} \tag{5}$$

where τ_i are the decay times and a_i the pre-exponential factors and *n* is the number of exponential terms. In addition, the fractional contribution (C_i) of each lifetime component is given by

$$C_i(\%) = \frac{a_i\tau_i}{\sum_{i=1}^{n} a_i\tau_i} * 100 \tag{6}$$

where, a_i represents the contribution of each exponential term at t = 0 and τ_i are the associated decay lifetimes.

The value of τ average (τ_{av}) was calculated by,

$$\tau_{av} = \frac{\sum_{i=1}^{n} a_i\tau_i * \tau_i}{\sum_{i=1}^{n} a_i\tau_i} \tag{7}$$

Chapter 3:

Results and discussion

3.1. Characterization of LUVs and GUVs

The LUVs used in the EET measurements were all produced using 2 stacked polycarbonate filters with 400 nm of pore size. LUVs hydrated with glucose aqueous solution and water were analyzed by DLS to obtain their average sizes and zeta potential values.

The average size of all formed LUVs containing only POPC and hydrated with glucose aqueous solution extruded with 2 polycarbonate filters with 400nm pore size (Figure 17) is around 200 nm (with PDI values varied between 0.2 and 0.3). It was noticed that, while with glucose, all LUVs maintained the same sizes (around 200 nm), with water LUVs obtained are bigger. LUVs with both probes and LUV-mix have average sizes that fall between LUV-NBD and LUV-Rho sizes (Figure 18).

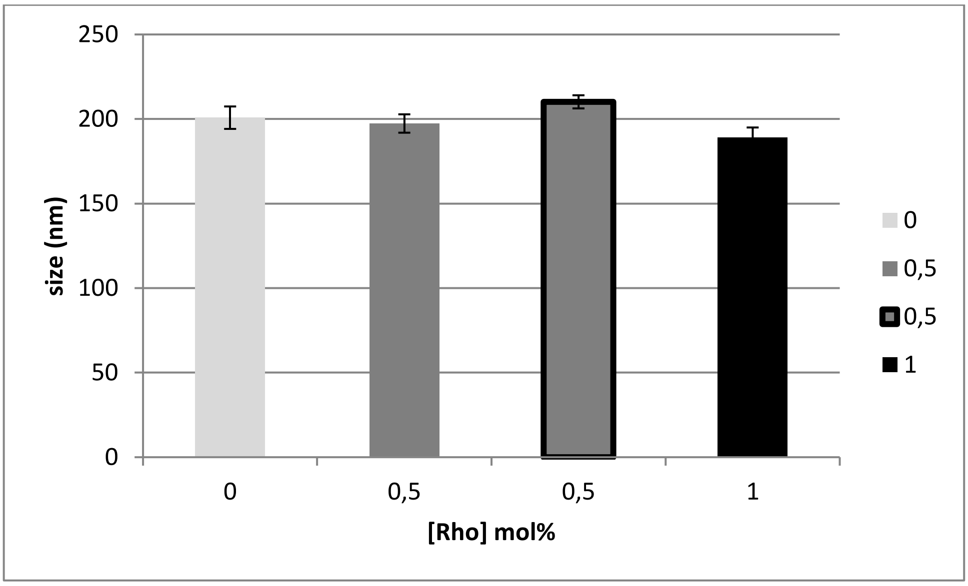

Figure 17. Average size (nm) of LUV-NBD (light grey), LUV-Rho (black), LUV-NBD-Rho (dark grey) and LUV-mix (grey with black outline) contacting only POPC in the bilayer and hydrated with glucose aqueous solution

Zeta potential values were also obtained. The results show that LUV-NBD, which are negatively charged, have a negative surface potential. LUV-Rho have positive values which means they are indeed positively charged. LUVs with both probes have values between these two charges, however it is observed that, for

LUVs hydrated with glucose aqueous solution, LUVs originally made with both probes have lower zeta potential than mixtures of LUVs (figures 19 and 20).

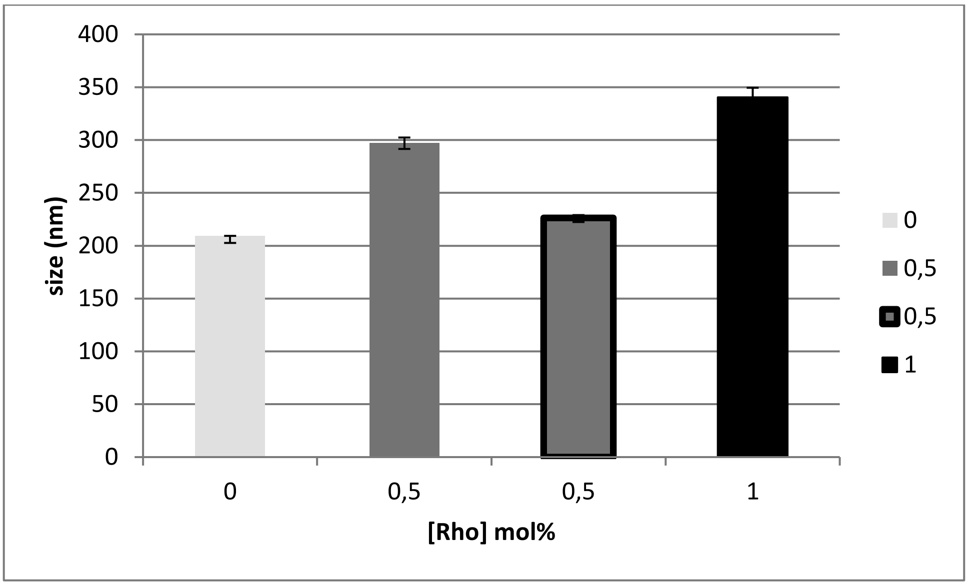

Figure 18. Average size (nm) of LUV-NBD (light grey), LUV-Rho (black), LUV-NBD-Rho (dark grey) and LUV-mix (grey with black outline) with composition in Table 2

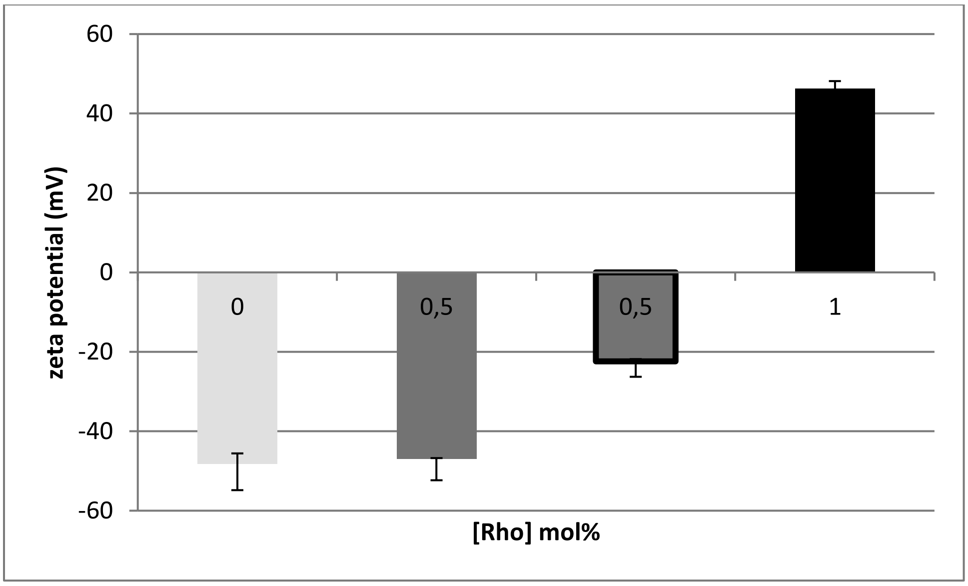

Figure 19. Zeta potential (mV) of LUV-NBD (light grey), LUV-Rho (black), LUV-NBD-Rho (dark grey) and and LUV-mix (outlined) hydrated with glucose aqueous solution

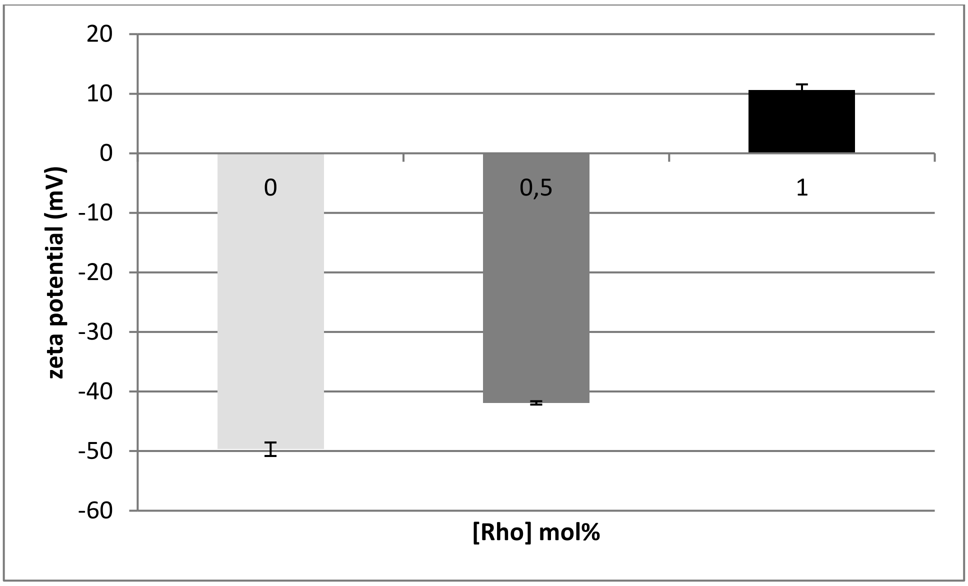

Figure 20. Zeta potential (mV) of LUV-NBD (light grey), LUV-Rho (black), LUV-NBD-Rho (dark grey) hydrated with water with composition in Table 2

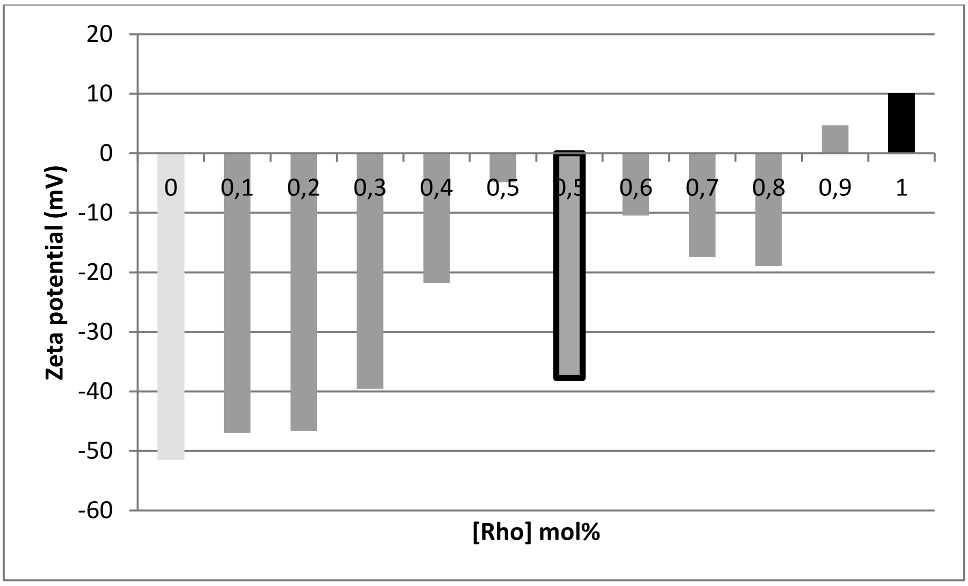

Figure 21. Zeta potential (mV) of LUV-NBD (light grey), LUV-Rho (black), LUV-NBD-Rho (outlined) and LUV mixtures with different proportions of LUV-NBD and LUV-Rho (grey) hydrated with water and composition indicated in Table 2.

The process of extrusions and FT in LUVs hydrated with water was followed by DLS (table 9).

Table 9. Size values after FT and extrusions in LUVs hydrated with water with composition in Table 2

	LUV-NBD		LUV-Rho		LUV-NBD-Rho	
	Av. Size (d.nm)	PDI	Av. Size (d.nm)	PDI	Av. Size (d.nm)	PDI
MLVs	1077	0,467	1012	0,481	1607	0,469
FT1	468,0	0,340	385,5	0,247	458,9	0,376
FT2	434,0	0,335	399,6	0,141	360,7	0,252
FT3	432,0	0,279	388,1	0,212	402,7	0,313
Extrusion 1	290,1	0,144	303,6	0,093	331,3	0,197
Extrusion 5	252,2	0,164	274,7	0,109	297,1	0,146
Extrusion 10	246,2	0,180	250,7	0,170	264,4	0,146

MLVs formed are all bigger that 1000 nm and right after the first FT cycle followed by and extrusion, the vesicles reduce considerably in size. After the 3 FT cycles and 10 extrusions, the three types of LUVs obtained are smaller than the 400 nm of the pore size.

GUVs were prepared based on Weinberger et al. 2013 method. This protocol was adapted, modifying how PVA was laid on the well surface, and the hydration solutions used.

Images obtained by confocal fluorescence microscopy revealed GUVs were successfully formed (figure 22).

These GUVs were constituted of POPC and 1% of probe, the lipid film was hydrated with 280 mM sucrose aqueous solution, diluted in glucose 280mM aqueous solution and allowed to sediment for 20 minutes. They are mostly unilamellar; however some multilamellar and multivesicular GUVs can be noticed too (pointed out with arrows 1 and 2, respectively). It is also curious to note that GUVs with Rhodamine (GUV-Rho) are bigger than GUVs with NBD (GUV-NBD).

The PVA film surface was also observed (figure 23). It can be noted that GUVs detached themselves creating circular empty shapes with no fluorescence. The formation of filaments by the PVA film is clearly seen on both examples.

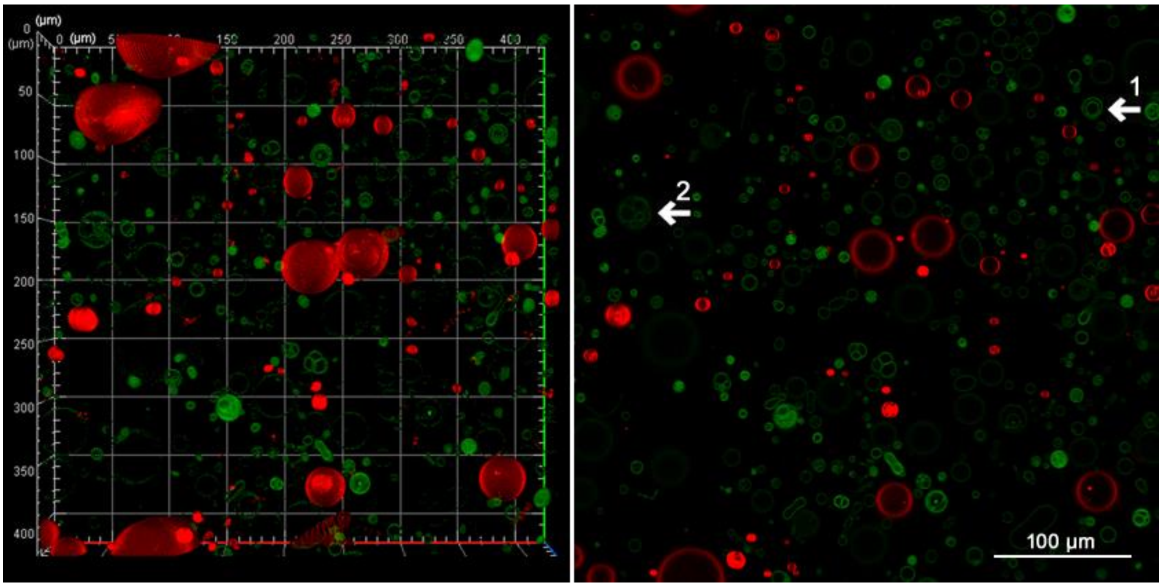

Figure 22. 3D view of GUV-NBD and GUV-Rho mixture (left); z-axis cut-section of the same sample (right)

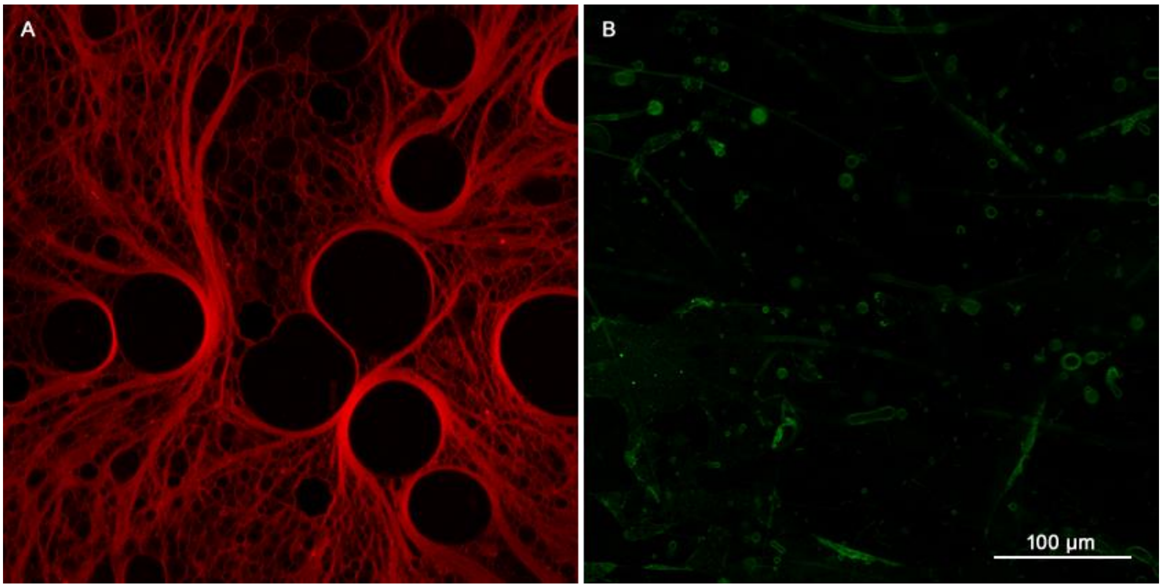

Figure 23. PVA surface (center of well). A: of GUV-Rho formation; B: of GUV-NBD formation

The same samples were also observed via conventional fluorescence microscopy (figure 24).

While confocal microscopy allowed viewing both channels by reconstitution from the software (because in reality, only one channel can be seen at one time), in conventional microscopy each channel was seen separately.

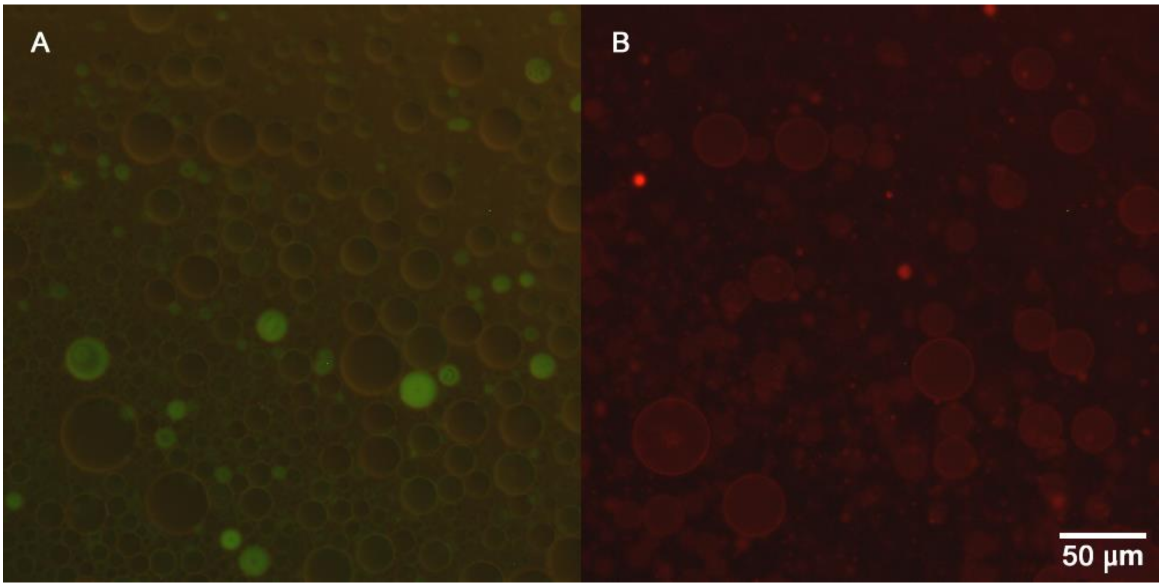

Figure 24. Conventional fluorescence microscopy imaging of GUV-NBD and GUV-Rho mixture

A. blue channel (GUV-NBD fluorescing in green) B. green channel (GUV-Rho fluorescing in red)

As opposed to the confocal microscopy technique, where images obtained from a cut-section are sharper and have high contrast, it is immediately noted that even though the images are less clear due to the bigger focal distance, the observation of GUVs is still very efficient. For this reason, only this microscopy technique was used for the following monitorings.

PVA surface was also observed via conventional fluorescence microscopy and the center of the well was compared to the borders (figure 25). It is curious to note that assembles of non detached smaller GUVs were found on the borders of the well of preparation.

To observe GUVs with conventional fluorescence microscopy, it was essential waiting for their deposition, as there was no cut-section to choose other than the bottom of the well for more and clearer GUVs. After diluting and waiting 2h, it was possible to achieve good contrast and sharpness (figure 26).

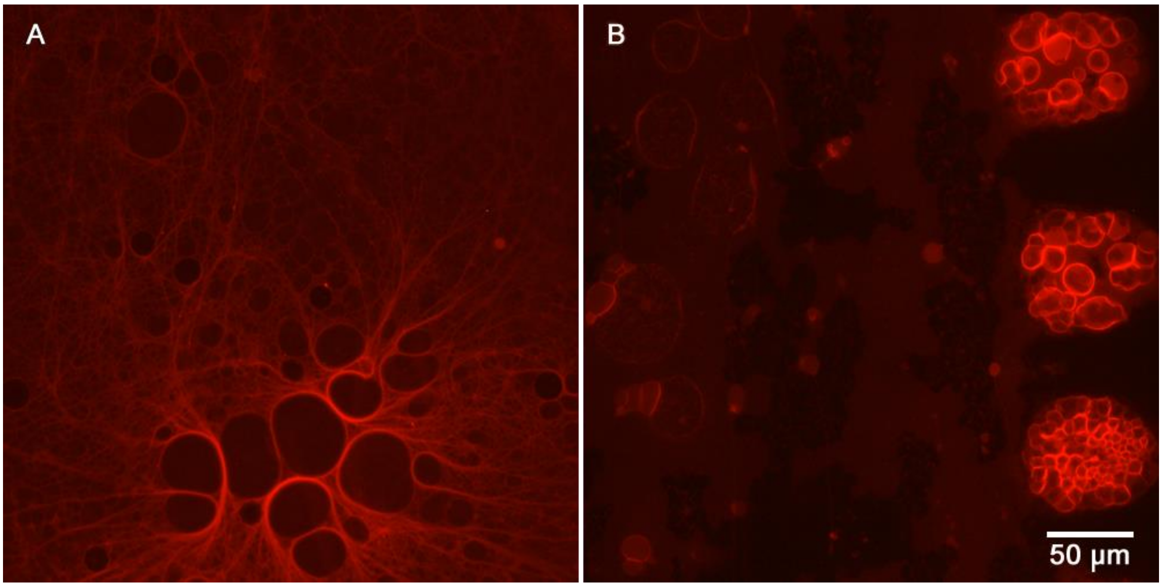

Figure 25. PVA surface imaging by conventional fluorescence microscopy. A. center of well; B. border of well

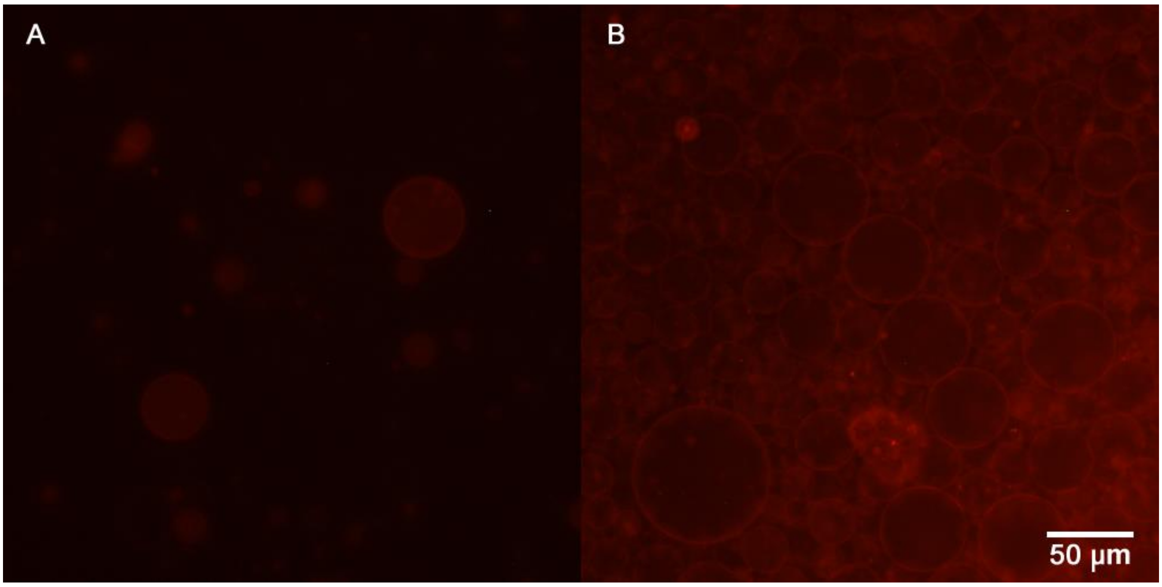

Figure 26. GUVs sedimentation
A: GUVs 20 minutes after dilution; B: after 2h

To enable drug encapsulation at a controlled physiological pH, we tried to prepare GUVs with phosphate added to the PVA solution (Na_2HPO_4 10mM). It was observed that there were very few GUVs formed and the lipid was found to be mostly laying on the PVA surface (Figure 27).

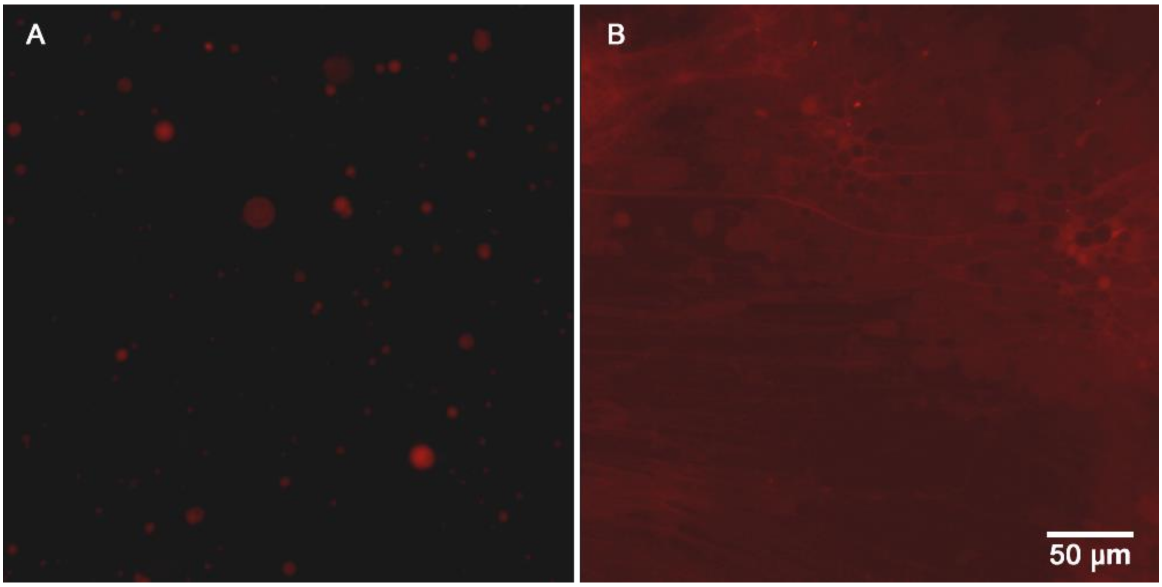

Figure 27. GUVs produced with phosphate. A. after 1:5 dilution with glucose solution; B. PVA film surface

Because the PVA film is negatively charged, a modification of the lipid composition (introducing negatively charged lipids) was also tried, in an attempt to facilitate lipid detachment from the polymer film. The results obtained with 10% POPS and 90% of POPC are shown in figure 28.

GUVs with only POPC in their constitution appeared to be bigger and obtained in higher quantity. Due to POPS being a negatively charged lipid, it can interact with the PVA surface by hydrogen-bonding interactions, thus complicating the process of release of the lipid which could be the reason why fewer GUVs were obtained.

For this reason, GUVs composition for the following essays only contained POPC.

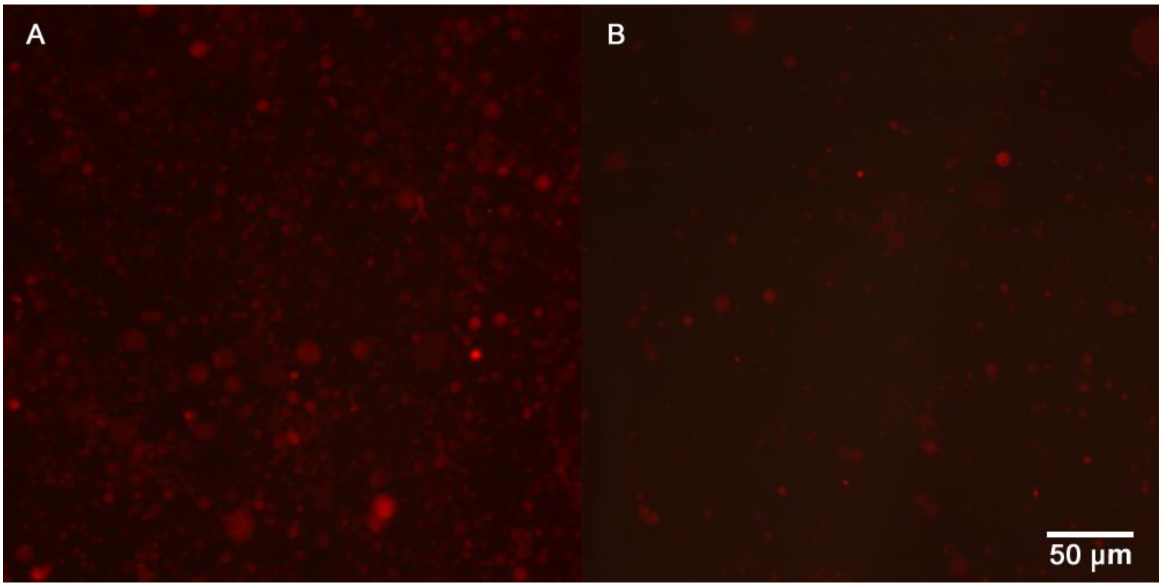

Figure 28. GUVs prepared from POPC (A) and POPC:POPS 9:1 (B)

GUVs formation appeared to be sensible to several conditions such as lipid composition, PVA application and turbulence during hydration. It was also noted during these essays that if the syringe touched the PVA film when applying the lipid onto its surface, it could slip under it and the GUVs formed would be smaller and lesser. GUVs with both probes (GUV-NBD-Rho) were also prepared (figure 29).

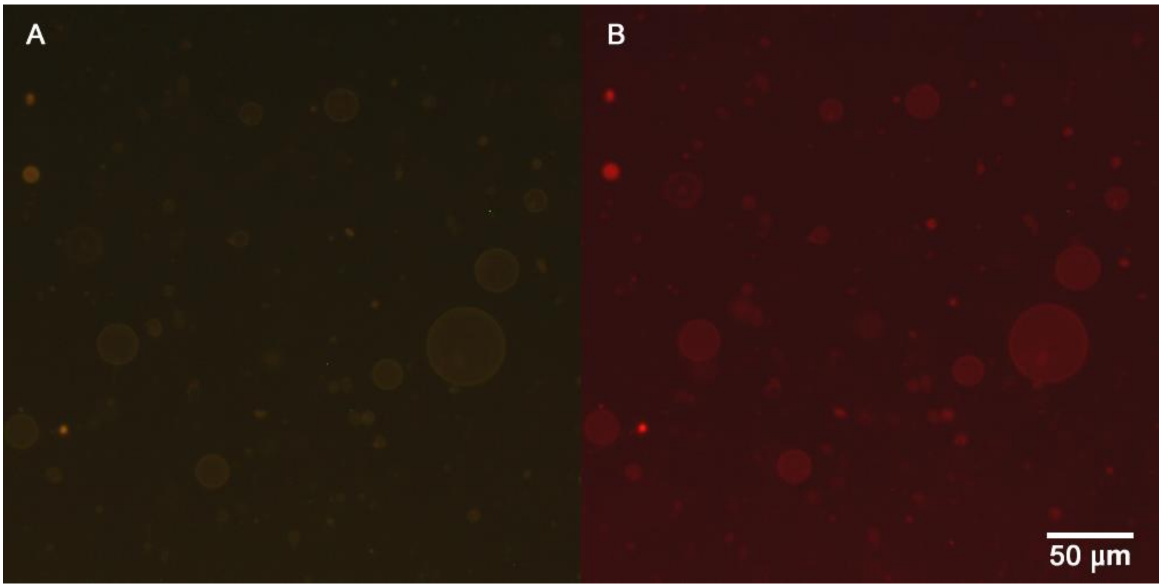

Figure 29. GUV-NBD-Rho observed via blue and green channels.
A. absorbing blue light; B. absorbing green light

GUVs with only NBD appear green using the blue channel and are not visible when using the green channel, while GUVs with only Rhodamine are not visible when observed with the blue channel and are red under the green channel. In contrast, GUVs marked with both probes are red when excited with both channels. Rhodamine's presence at short distances nearby in the membrane, results in energy transfer from NBD to Rhodamine, the latter fluorescing in the red (manifestation of FRET occurring). This shows that at the local concentrations of Rhodamine used (1 mol%) efficient energy transfer from NBD to Rhodamine is occurring.

Finally, GUVs hydrated with a sucrose aqueous solution containing FITC-dextran were produced. FITC-dextran was chosen for its high molecular weight and size, so its permeation through the bilayer is slower than fluorescein. The permeation is also not dependent of the pH. These GUVs contained Rhodamine in their bilayer to allow their clear visualization using the green light source while FITC-dextran could be seen using the blue light source.

To separate bigger GUVs from smaller ones, centrifugation (using several times at the same rpm) was applied to the samples to reduce the waiting time of sedimentation (figure 30).

Using the green channel to view GUVs, controls with 1:5 and 1:25 dilutions with glucose aqueous solution served to demonstrate that while the supernatant of the first dilution contains large GUVs, the latter shows the presence of smaller sized ones, which indicates that by diluting and collecting the pellet after waiting a certain time, it is possible to collect only the bigger GUVs.

In order to obtain mostly the bigger GUVs, several times of centrifugation were applied to the pellet of GUVs samples diluted 25 times. The use of these procedures visibly separated smaller GUVs from bigger ones at first, however bigger ones are less seen as time of centrifugation increased. For that reason, comparing to the separation done by gravitation force and waiting after the dilution, centrifugation was not used for the following experiments.

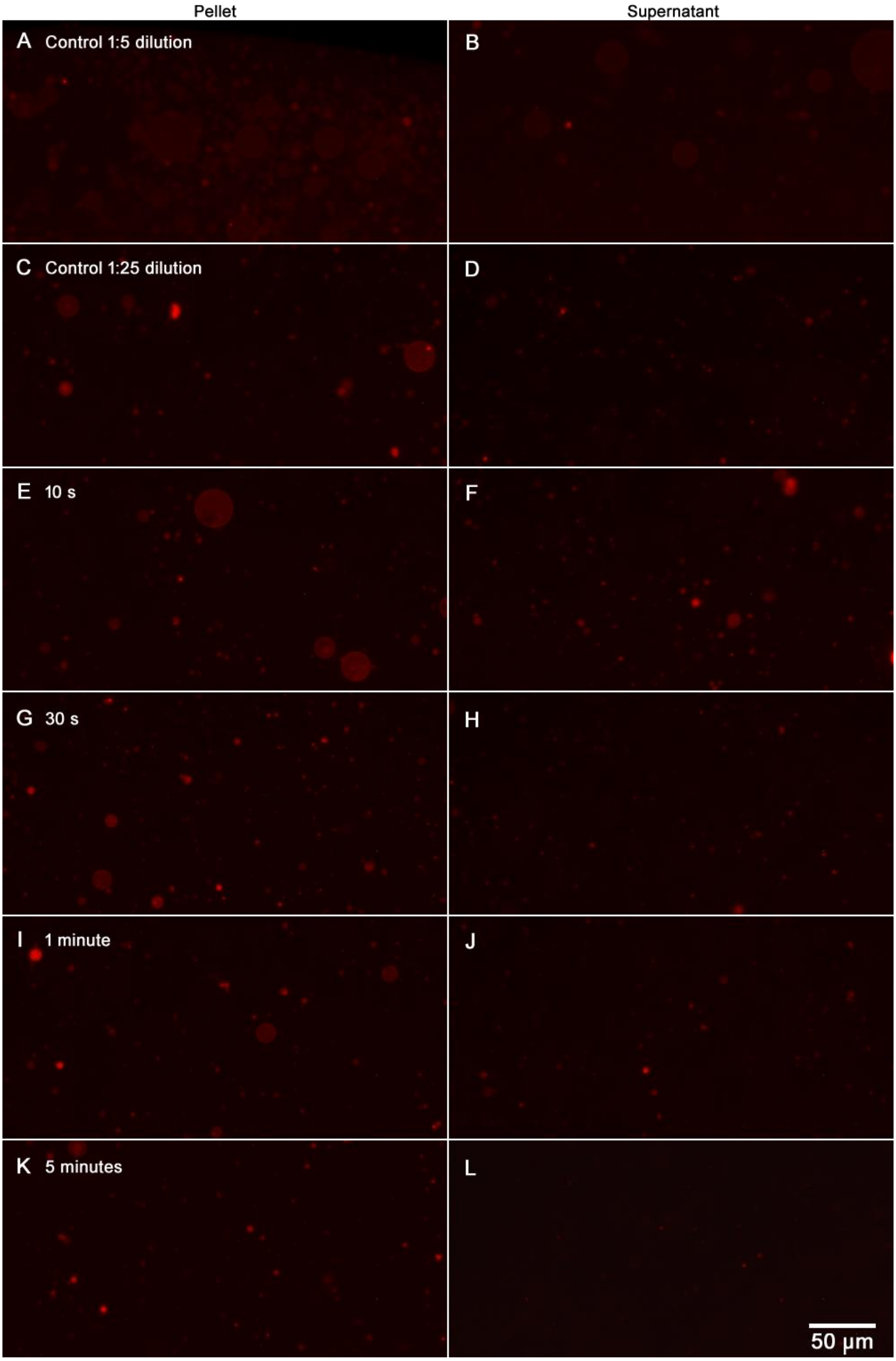

Figure 30. Centrifugation effect on GUVs
Left column: “pellet”, right column: “supernatant”. A,B: Control (1:5 dilution); C,D: Control (1:25 dilution); E,F: 10s; G,H: 30s; I,J: 1 min; K,L: 5 min

With the blue light source, immediately after the preparation of the GUVs (no dilution) the inner and outer media have the same fluorescence intensity as both have the same concentration of dye. To tackle this issue, a dilution study was done (figure 31).

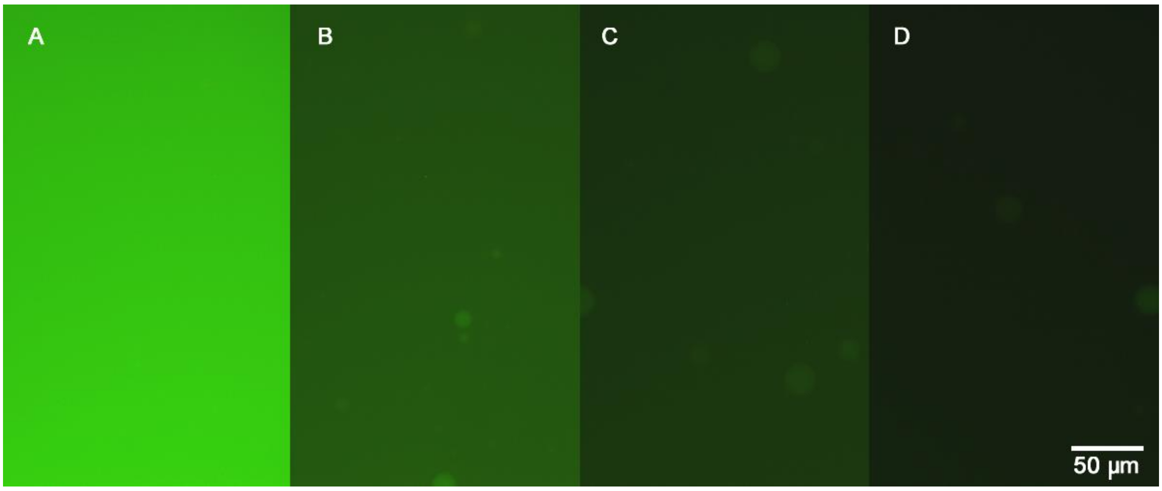

Figure 31. Dilution of GUVs hydrated with FITC-dextran
A – 1:5 dilution; B - 1:25 dilution; C - 1:50 dilution; D - 1:125 dilution

A 1:50 dilution with a waiting time of 45 minutes for sedimentation was chosen as it provided the clear contrast between the fluorescence of GUVs containing FITC-dextran inside and the external medium. A bigger dilution such as 1:125 gives the best contrast however it required more time for GUVs to deposit in a higher volume.

3.2. Fusion essays with LUVs

Studies with LUVs were done because although they are smaller than GUVs and can’t be observed through microscopy, they are homogenous in size and composition and their curvature is similar. For this reason they can be used for steady-state and time-resolved fluorescence spectroscopy.

LUVs composition included different lipids in various proportions. Firstly, LUVs with only POPC hydrated with an aqueous solution of glucose were used and samples of LUVs marked with NBD (LUV-NBD), LUVs marked with rhodamine (LUV-Rho), LUVs marked with equal percentages of both probes

(LUV-NBD-Rho) were prepared. A 1:1 mixture of LUV-NBD/LUV-Rho (LUV-mix) was also prepared to evaluate the energy transfer from NBD to Rhodamine.

3.2.1. Steady-state measurements

To obtain the fluorescence intensity values for the calculation of the energy transfer efficiency, spectra data were obtained taking in account NBD and rhodamine excitation and emission. For that, emission spectra with excitation at 450 and 568 nm (x450 and x568) and excitation spectra collecting fluorescence at the maximum emission at 530 and 590 nm (m530 and m590) of LUV samples were obtained (figure 32).

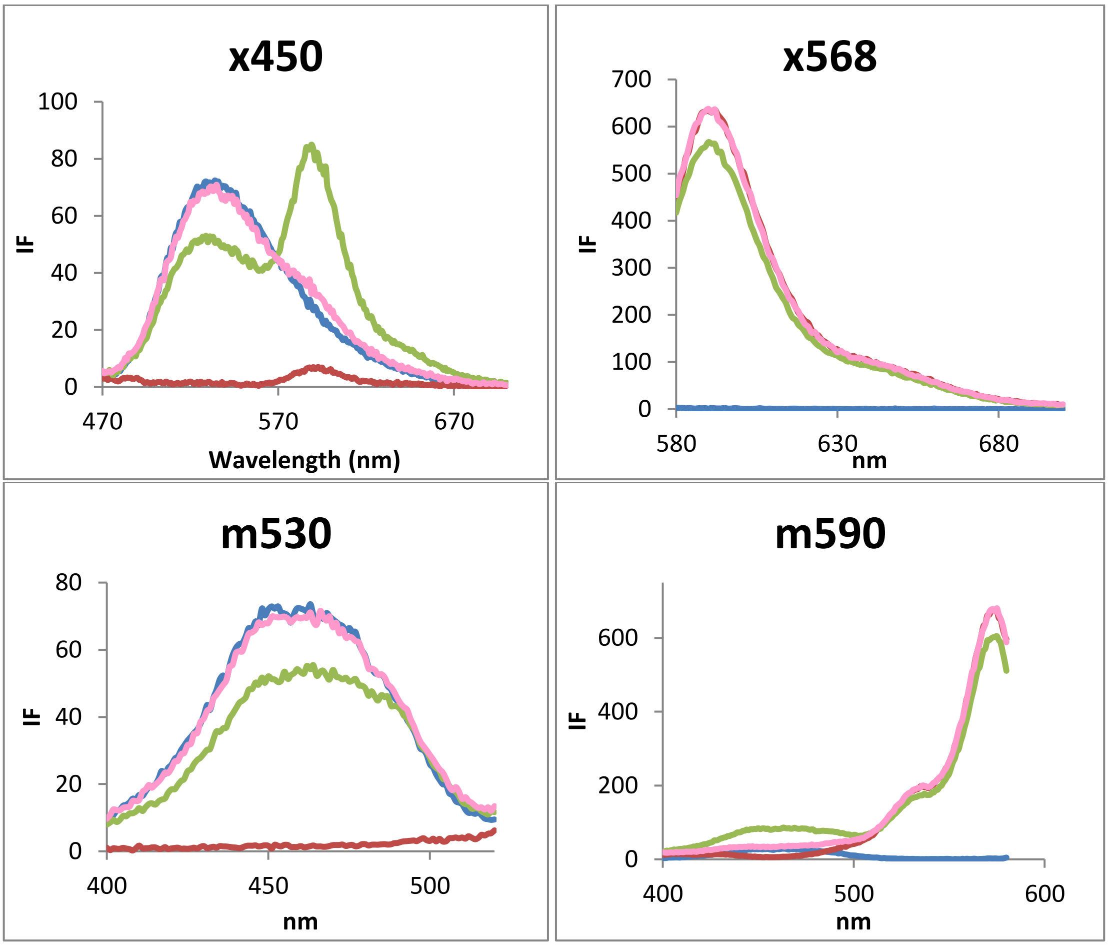

Figure 32. Spectra data of LUVs suspensions containing only POPC in the bilayer and hydrated with glucose aqueous solution
LUV-NBD (blue), LUV-Rho (Red), LUV-NBD-Rho (green) and a 1:1 mixture of LUV-NBD and LUV-Rho (pink)

With these spectra data we notice that with excitation at 450 (x450) the emission of NBD has its maximum at around 530 nm and rhodamine's at 590 nm. LUVs containing only NBD (LUV-NBD) show high fluorescence intensity at 530 nm, while for LUVs containing only Rho (LUV-Rho) the fluorescence intensity (at 590 nm) is very small. For the LUVs prepared with NBD and Rho (LUV-NBD-Rho) the fluorescence intensity at 530 nm is smaller than for NBD only, while that at 590 nm is much higher. This reflects the efficient energy transfer from NBD to Rho at the high local concentration of the acceptor (Rho at 0.5 mol%). The fluorescence from the physical mixture of LUVs containing only NBD and only Rho (LUV-mix) just after preparation corresponds to the sum of the fluorescence from the LUVs with only one of the probes, indicating that no significant exchange of probes between the two LUV populations as occurred. For energy transference studies, LUV-NBD-Rho serve as the maximum condition of efficiency of energy transfer between NBD and Rho.

Using excitation at 568 (x568), the collected emission of LUV-NBD was nonexistent; however rhodamine's emission has its highest fluorescence intensity in LUV-Rho at 590 nm. For LUV-mix, this value is practically equal while in LUV-NBD-Rho the intensity decreases.

By collecting the excitation when the maximum emission is at 530 nm (m530), LUV-NBD show an intense band with an estimated maximum at 465 nm. In LUV-NBD-Rho that value is lower and in LUV-mix it is almost equal to LUV-NBD.

At maximum emission 590 nm (m590), the excitation spectra showed LUV-Rho and LUV-mix with very similar profiles, with their maximum at around 574 nm. LUV-NBD have a small intensity band with a maximum around 465 nm and LUV-NBD-Rho shows a higher intensity of this band but a lower value of rhodamine's intensity.

With all of those observations, each condition could demonstrate that at x450, the $\frac{IF_{530}}{IF_{590}}$ ratio in LUV-NBD-Rho is lower than 1 while in the LUV-mix this value is higher than 1; at x568, IF_{590} of LUV-NBD-Rho is lower than in LUV-mix; at m530, IF_{465} of LUV-NBD-Rho is lower than in LUV-mix; and at m590, $\frac{IF_{574}}{IF_{465}}$ ratio is lower in LUV-NBD-Rho. In account of that, the emission of NBD (exciting at 450) and excitation of rhodamine (collected by maximum emission at 590) were chosen as the conditions that could give the most information.

A first test to evaluate lipid mixing in the sample containing two distinct LUV populations (LUV-mix) was done by applying FT cycles and several PA waves laser fluencies, with the primary objective of identifying in which conditions fusion or another physical event (lipid rearrangement into new vesicles mixing both original lipid pools) would take place in these LUVs. Spectra data was then analyzed to determine the EET resulting from the physical procedures done to the LUVs mixtures (figure 33).

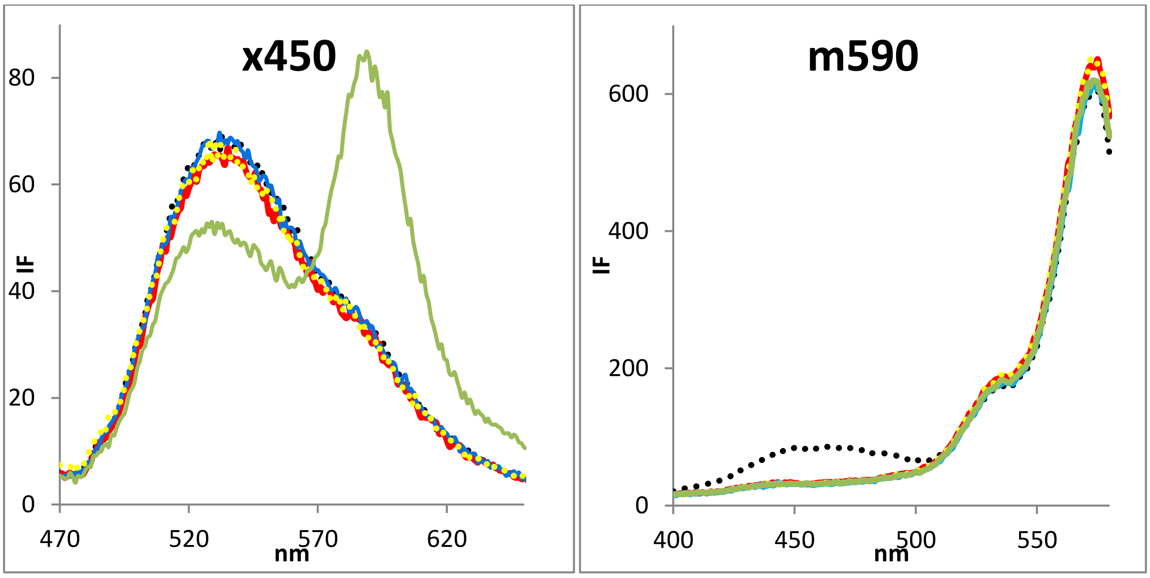

Figure 33. Spectra data at x450 (left) and m590 (right)

LUV-mix of LUVs of POPC hydrated with glucose aqueous solution (control, dotted in black), after PA waves application (100 (red) and 400 (blue) mJ/cm^2 for 10 minutes), after a FT cycle (dotted in yellow) and LUV-NBD-Rho (green)

The energy transfer was firstly assessed by the ratio between IF at 530 and 590 of the emission spectra at 450 excitation in several samples of LUV-mix (control is obtained right after the mixing of LUV-NBD and LUV-Rho at 1:1 ratio, LUV-mix L100-10 is the mixture submitted to laser with 100 mJ/cm^2 energy during 10 minutes and L400-10 is using 400 mJ/cm^2 and LUV-mix FT is the mixture submitted to one cycle of freeze and thaw) and compared to the value of LUV-NBD-Rho (table 10).

EET values (obtained by applying Equation 2, considering the IF at 530 with both donor and acceptor and the IF with only donor) show that the effect of PA waves and FT were practically inexistent in these LUVs, as the values are essentially the same for all LUV-mix samples and different from that of LUV-NBD-Rho, where FRET occurs.

Table 10. Calculated IF ratios at x450 and EET values

	$\frac{IF_{530}}{IF_{590}}$	EET
LUV-NBD-Rho	**0.630**	**0.29**
LUV-mix Control	2.04	0.07
LUV-mix L100-10	2.07	0.08
LUV-mix L400-10	2.12	0.06
LUV-mix FT	2.10	0.04

Like LUV-NBD-Rho, where the maximum of EET occurs, applying FT cycles to LUV-mix would predictably produce LUVs with both probes in their membrane. However, this doesn’t happen as these LUVs were hydrated with an aqueous solution containing glucose. Glucose is a cryoprotectant and it represses ice formation during freezing. Freeze and thaw causes physical disruption of the lipid-bilayer as a result of ice crystal formation,[28] but using a cryoprotectant such as glucose or sucrose to hydrate LUVs inhibits the mixing of LUVs inhibits the formation of said crystals.

In consequence of the previous results, LUVs preparation suffered some alterations. LUVs were hydrated with water instead of glucose aqueous solution and the lipid composition was also modified. To promote the approach between LUVs in the mixture, the overall lipid charge of the membranes were changed (composition in Table 2) to negative for LUV-NBD by adding 5% of POPS, and positively charged for LUV-Rho by adding 5% of DDAB. Moreover, 20% of POPE was also added to both LUVs, as this is a lipid with a different shape than POPC, having a smaller headgroup. The presence of the inverted cone shaped lipid in these is expected to facilitate the fusion/fission processes by decreasing the hydration force[72] and stabilizing high energy intermediate states.[73]

The stability of LUV-mix was assessed over time by following spectra data from emission spectra exciting at 450 nm (figure 34).

To assess that the mixture of LUV-NBD and LUV-Rho is stable over time, the ratio $\frac{IF_{530}}{IF_{590}}$ was calculated (table 11) and compared to the ratio given by LUV-NBD-Rho.

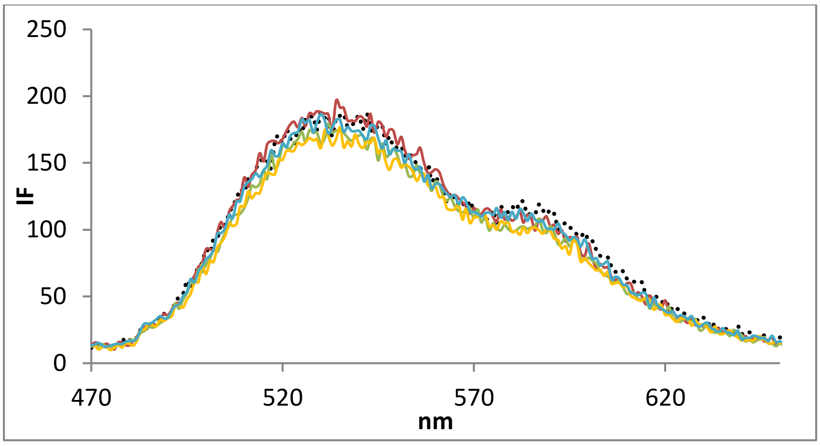

Figure 34. Emission spectra of LUV-mix at different time points (t=0 black dotted, t=1h in red, t=2h green, t=3h orange and t=4h blue)

Table 11. Variation of IF (530/590) ratio at x450 of LUV-mix over time (t)

t (h)	$\frac{IF_{530}}{IF_{590}}$
0	1.55
1	1.69
2	1.55
3	1.59
4	1.60

The average value of $\frac{IF_{530}}{IF_{590}}$ ratio for LUV-mix is 1.60 and comparing it to the ratio obtained by LUV-NBD-Rho, 0.338 (indicated in table 12), the value is over 1 and thus corroborates that the mixture is stable without any action submitted to them (at least for 4h and not showing tendency to change).

Freeze and thaw was then applied to the LUV-mix and compared to a LUV-NBD-Rho sample and the effect was evaluated after each performed cycle (figure 35).

After the first freeze and thaw cycle applied to the LUV-mix, the intensity of the NBD emission drops and rhodamine's increases. The more FT cycles, the more intense is rhodamine's fluorescence and the ratio between those two bands becomes closer to LUV-NBD-Rho values. $\frac{IF_{530}}{IF_{590}}$ and $\frac{IF_{574}}{IF_{465}}$ ratios were calculated and compared to LUV-NBD-Rho samples which were also submitted to FT cycles (table 12).

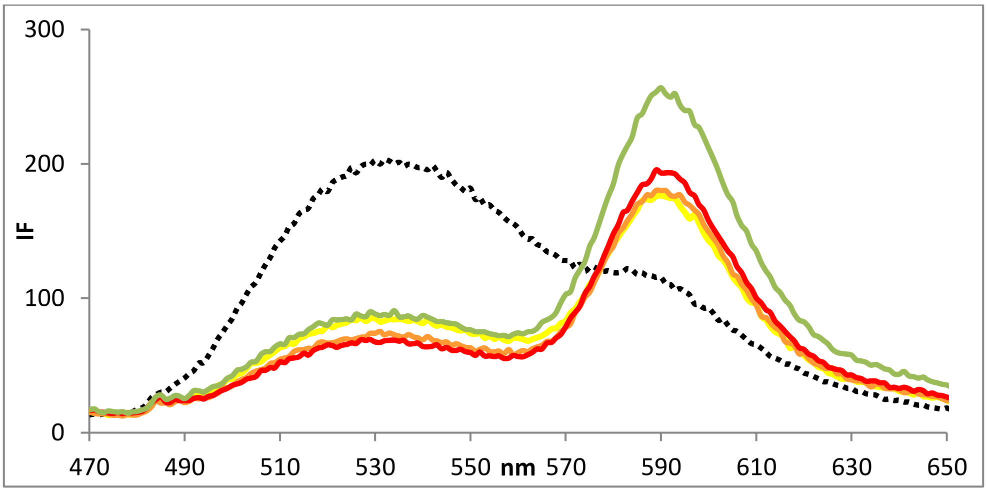

Figure 35. Spectra data at x450 of LUV-mix after each FT cycle and LUV-NBD-Rho as final control

LUV-mix of LUVs of composition from Table 2 (control, dotted in black), after 1 FT cycle (yellow), 2 FT cycles (orange), 3 FT cycles (red), LUV-NBD-Rho (green)

After 3 cycles of FT, LUV-mix $\frac{IF_{530}}{IF_{590}}$ ratio value is practically equal to the value for LUV-NBD-Rho. This means that the fusion between LUV-NBD and LUV-Rho was successful and there's energy transfer between the probes by fusion of the pools. It is also noticed that after applying FT to LUV-NBD-Rho samples, the values stay approximately the same because the quantity of NBD and Rho in the lipid pool stays the same.

It was decided to perform 5 cycles of FT in the following essays to assure complete mixing between LUVs, even though after 3 FT the value of EET is 0.65

and for LUV-NBD-Rho it is 0.59, the ratio in LUV-mix was still higher than for LUV-NBD-Rho.

Table 12. Effect of FT cycles in IF(530/590) ratio for LUV-mix and LUV-NBD-Rho

FT cycles	$\frac{IF_{530}}{IF_{590}}$		EET	
	LUV-Mix	LUV-NBD-Rho	LUV-Mix	LUV-NBD-Rho
0	1.6	0.35	-0.04	0.54
1	0.48	0.34	0.56	0.56
2	0.42	0.34	0.61	0.58
3	0.36	0.33	0.65	0.59

To quantify the EET that could occur from PA waves application on LUVs, a calibration curve was designed. In those experiments, if fusion occurs it is not expected to generate LUVs with equal proportion of the two probes as it may involve several LUVs.

To access the effect of the acceptor fraction in the EET in the LUV-mix fusion, several samples of LUV-mix with different proportions of LUV-NBD and LUV-Rho were prepared. The spectra data was obtained and the discussion was focused on the results at m590, before and after FT (figure 36).

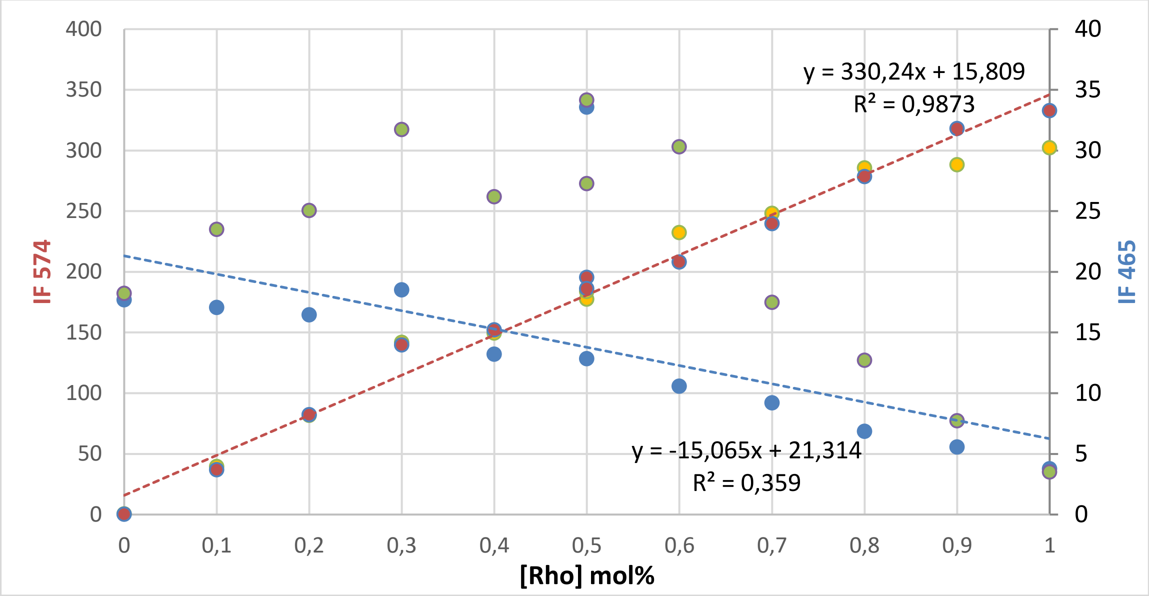

Figure 36. Variation of IF 574 and IF 465 at m590 of LUV mixtures

(LUV-mix: red (IF 574) and blue (IF 465); LUV-mix FT: orange (IF 574) and green (IF 465), the dotted lines are linear fits to the LUV-mix before FT)

The variation of IF_{574} and IF_{465} before submitting LUVs mixtures to FT cycles was found to vary linearly with the concentration of acceptor. As the fraction of LUVs containing the acceptor Rhodamine increases (the fraction of those containing the donor NBD decreases), the fluorescence intensity from Rho, when exciting at 574 nm increases (that from NBD, when exciting at 465 nm decreases).

After FT, no significant effects are observed on the fluorescence intensity when exciting Rhodamine directly (IF 574 nm), but a large increase is observed when Rhodamine is excited through energy transfer from NBD (IF 465 nm).

The $\frac{IF_{574}}{IF_{465}}$ values obtained before and after FT increase when increasing acceptor concentration. The difference between the two curves is linear, which shows the concentration dependence of the EET. Taking in account the Equation (3), the distance between donor and acceptor correlates to the concentration, because at higher concentrations, the distance, *r*, decreases and in consequence, the energy transfer increases.

When in presence of acceptor, NBD transfers its energy through FRET mechanisms. After FT, NBD that was in LUV-NBD is closer to Rhodamine due to the fusion of the vesicles. At lower LUV-Rho fractions, there are too many donors and very few acceptors to transfer energy to, meaning that the energy transfer is barely effective.

The $\frac{IF_{574}}{IF_{465}}$ ratio before and after FT was calculated (figure 37).

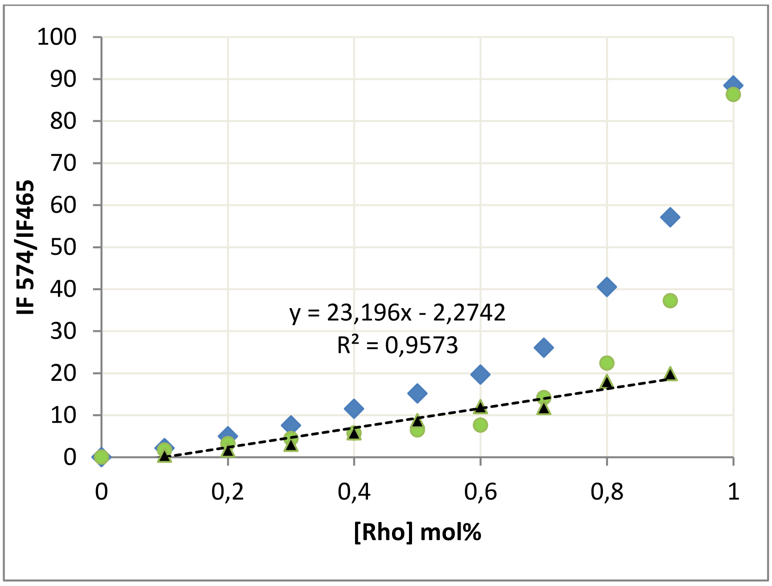

Figure 37. Variation of IF(574/465) before (blue) and after FT (green) in LUVs mixtures, LUV-NBD (0 mol% [Rho]) and LUV-Rho (1 mol% [Rho]) in function of rhodamine concentration and difference (with linear tendency line) between the two sets of data (black)

The same analysis was done using emission data collected from excitation at 450 nm (figure 38).

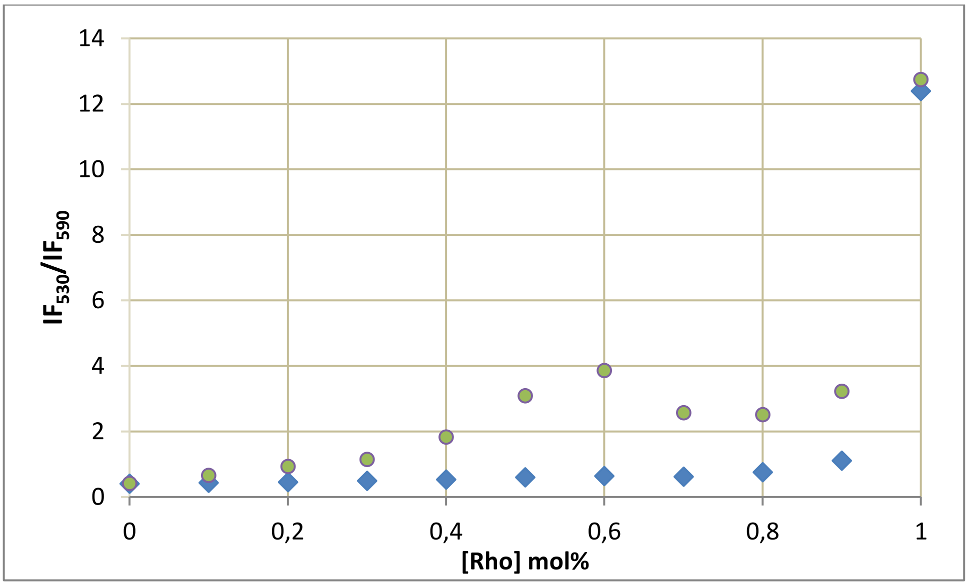

Figure 38. Variation of IF590 at x568 before (blue) and after FT (green)

3.2.2. Steady-state fluorescence measurements

The efficiency of energy transfer for the different mixtures before and after FT was calculated using data from excitation spectra at 450 nm. IF_{530} was predicted through NBD's concentration, assuming it is linear, considering as reference IF_{530} at x450 when the sample contained only LUV-NBD ($[NBD]_{total}$), by

$$IF_{530} = IF_{530\ [NBD]total} * \frac{[NBD]}{[NBD]_{total}} \tag{8}$$

$\frac{IF_{da}}{IF_d}$ was then calculated by $\frac{IF_{530x450}}{IF_{530}}$ and using the Equation 2, the EET was obtained (figure 39).

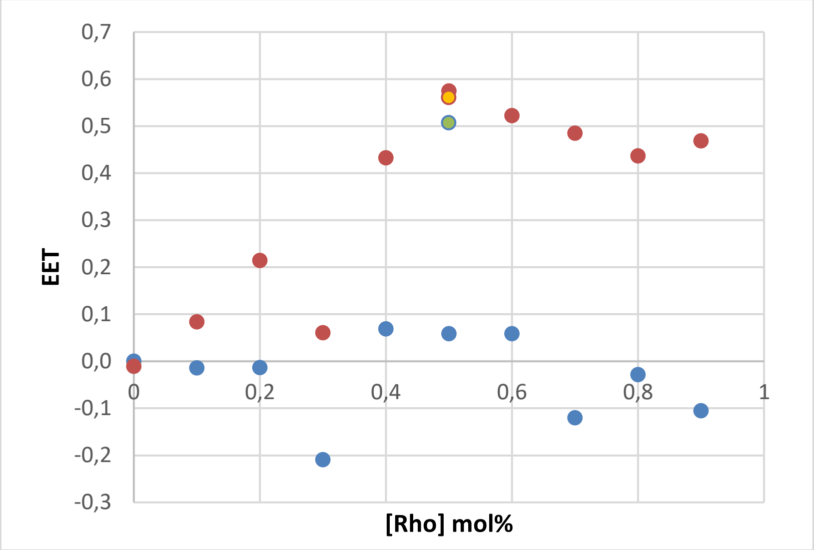

Figure 39. EET values obtained by predicted IF530 from NBD before (blue) and after FT (red)

EET values obtained for mixtures before FT procedure are close to being 0 (the average of these values being equal to 0). After FT, EET values tend to increase until [Rho] mol% = 0.5, where the maximum EET was obtained at with 0.52. It is observed that after the 1:1 fraction, for higher rhodamine fractions, EET starts to decrease. According to the Equation 3, the EET is dependent of the distance between donor and acceptor. The higher is the concentration of acceptor, the closer donors will be. However, at more than 0.5 mol% of NBD there is not enough donor to donate energy to the acceptors present in the medium, so that reflects in less energy transfer.

3.2.3. Time-resolved fluorescence measurements

FRET can also be measured by fluorescence lifetimes. This methodology is advantageous because it is not affected by the concentration of the sample, which means it is not sensitive to the evaporation of solvent, and also enables measurements in samples that contain different local concentrations of donor and acceptor. With steady-state measurements only the average value of EET can be obtained.

Using SAND program, decays were deconvoluted. The decay profile of a sample containing only LUV-NBD is shown in Figure 40.

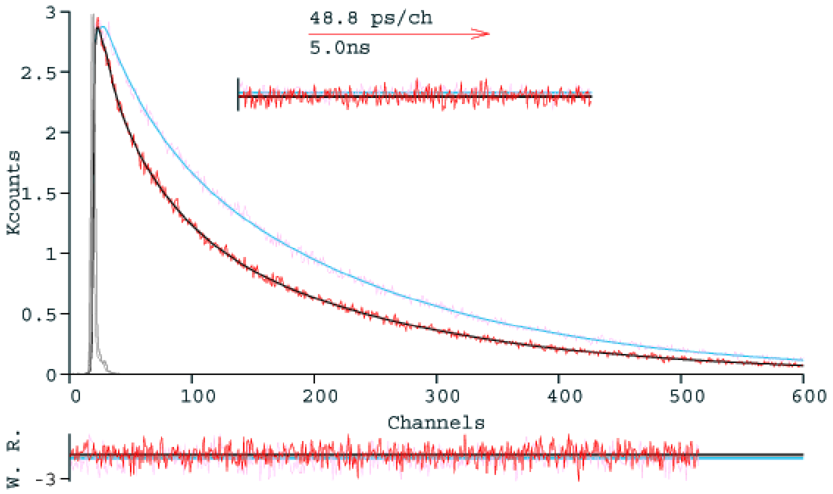

Figure 40. Typical decay profile of LUV-NBD (blue) and LUV-Mix (red)

LUV-NBD and LUV-Mix in sucrose aqueous solution. Experimental results and fitting done by SAND program

The experimental decay was fitted with a tri-exponential function, which is also observed in results from literature.[74] The first lifetime is shorter due to dispersion and the other two correspond to the fluorescence of NBD.

The values of τ1, τ2, τ3 and respective coefficients a1, a2 and a3 were obtained for all LUV mixtures samples, the sample containing only LUV-NBD and the sample containing only LUV-NBD-Rho (Figure 41).

In samples with donor and acceptor τ1, which has a lower lifetime, increases with the percentage of LUV-NBD-Rho while τ3 which has the longest lifetime, decreases due to FRET occurring.

EET values were obtained using the equations 2, 6 and 7 and were displayed in the figure 42.

It can be observed that at maximum of LUV-NBD-Rho presence, EET is 0.42 for LUVs BS and 0.43 for LUVs AD, while comparing them to the measurements done by steady-state fluorescence; they are 0.54 and 0.57, respectively. These values obtained by time-resolved measurements are closer to the maximum value obtained for LUVs hydrated with water who were successfully mixed by FT (0.52), which led us to conclude that time-resolved results could be validated for LUVs hydrated with sucrose aqueous solution.

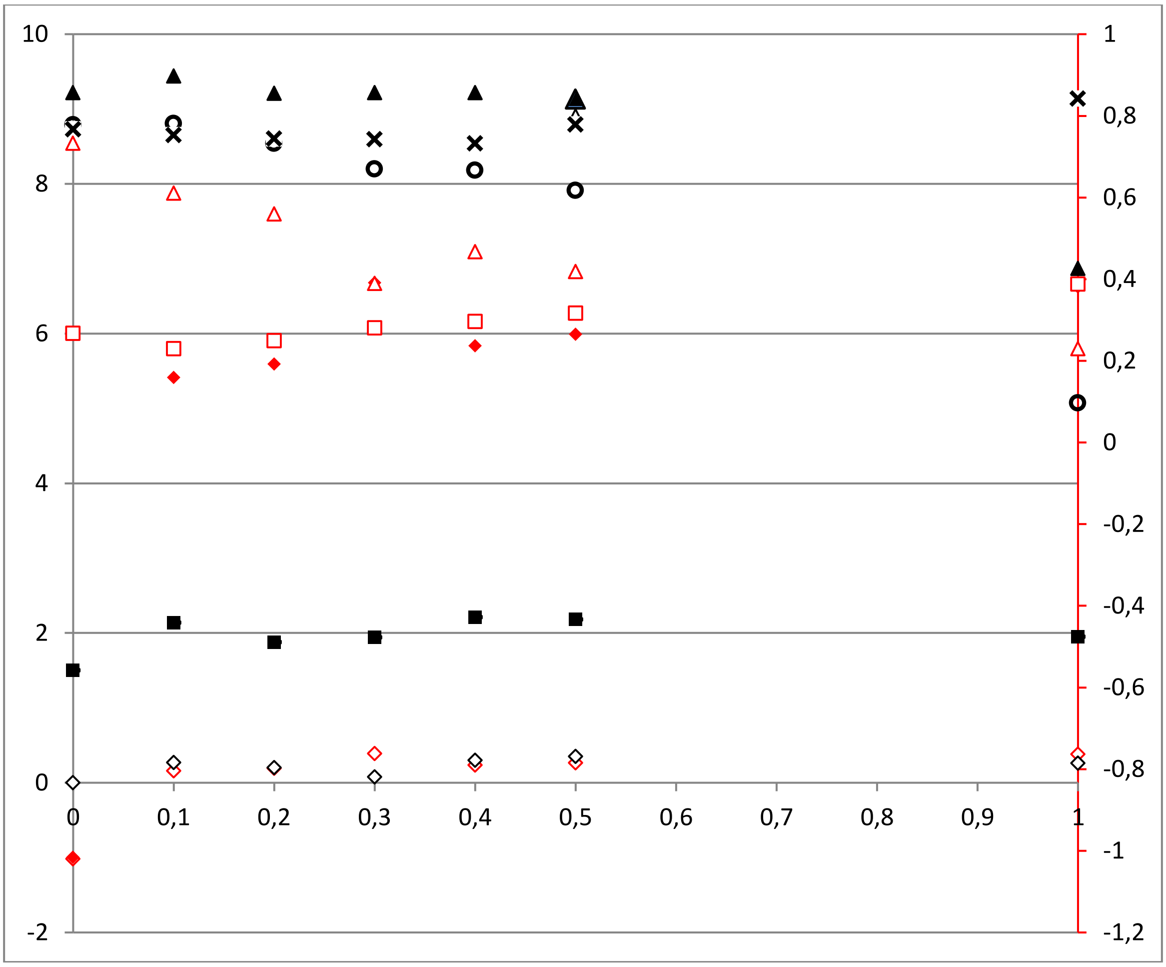

Figure 41. τ1 (◆), τ2 (■)and τ3 (▲) (black) and a1 (◆), a2 (■)and a3 (▲) (red) values obtained for LUVs AD (empty markers) with τ average (x) LUVs BS (filled) with τ average (o) at different LUV-NBD-Rho percentages.

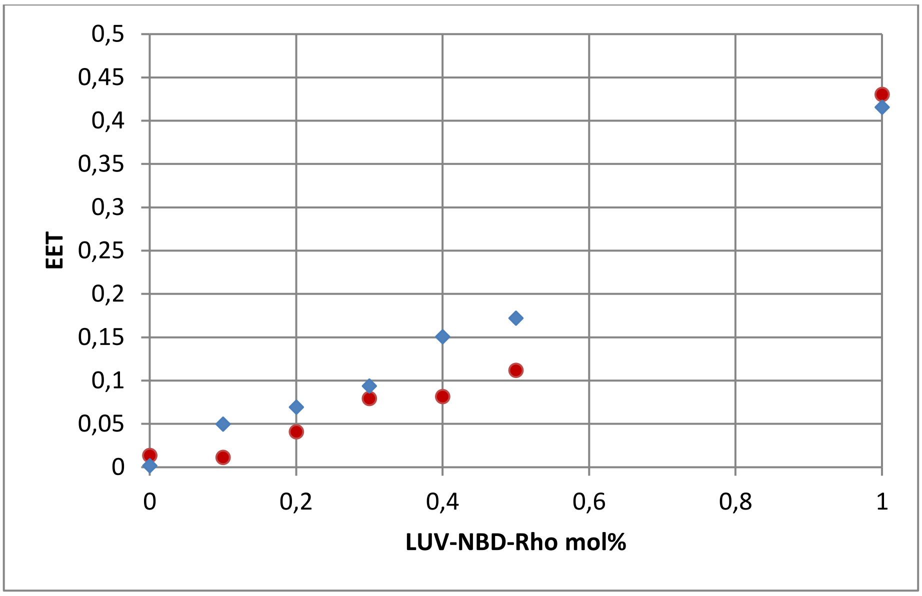

Figure 42. Variation of EET with different percentages of LUV-NBD-Rho LUVs AD (red), LUVs BS (blue)

3.2.3. PA waves effect

Samples of LUVs mixtures both of LUVs AD and LUVs BS (compositions in tables 4 and 5, respectively) in a 1:1 LUV-NBD:LUV-Rho ratio were submitted to PA wave application and time-resolved measurements were obtained to calculate the EET (Table 13). According to the results, energy transfer is not observed when applying photoacoustic waves to the LUV mixtures of both LUVs BS and LUVs AD (the latter showing negative EET values).

Table 13. EET values after applying PA waves on LUV mixtures (1:1 LUV-NBD:LUV-Rho) done with LUVs AD and LUVs BS

Sample	LUVs AD	LUVs BS
C0	-0.03	0.02
C10	-0.02	0.03
C20	-0.03	0.03
L100-10	-0.04	0.02
L100-20	-0.04	0.01
L200-10	-0.04	0.02
L200-20	-0.02	0.03

The effect of PA waves was also studied by steady-state measurements collecting emission spectra data at maximum excitation 450 nm. The samples used were mixtures of LUVs with charge (LUVs AD) ones that contain POPS and NBD and others that contain DDAB and rhodamine hydrated and diluted in sucrose aqueous solution; and mixtures of LUVs that contain Biotin (LUVs BS) were hydrated with aqueous sucrose solution and were diluted in Streptavidin solution and aqueous sucrose solution.

Analyzing first LUVs BS (Figure 43), it is observed that after applying PA waves there is an increase in the intensity at 530 nm (NBD maximum emission). This happens when increasing the time exposure to the stress waves. On LUVs AD, the 200 mJ/cm^2 laser fluency was also tested and also showed an increase of intensity after the application (Figure 44). This increase of intensity seen on both experiments could have been due to evaporation of the LUVs sample on top of the setup, so a cover glass was installed on top of it to create a barrier that would prevent that of happening. The results show that the intensity after PA waves application using the cover glass is less, because some evaporation was avoided. It is therefore not correct to calculate EET in these conditions (values would be negative).

Using the same LUVs, mixtures of LUV-NBD, LUV-Rho and LUV-NBD-Rho were prepared to allow the interpretation of the changes in the fluorescence intensity observed upon application of the PA waves. For that, a calibration curve was performed representative of increasing efficiencies in LUV fusion. Because the hydration solution contains sucrose, FT would not be effective to promote the fusion. In order to observe energy transfer, increasing proportions of LUVs containing both donor and acceptor (LUV-NBD-Rho) were mixed with LUVs containing only donor and only acceptor (at 1:1 proportions). In this way, the overall concentration of donor and acceptor is always the same, but at different fractions of LUVs containing both probes. The calculated EET for LUVs AD and LUVs BS are shown in Figure 45.

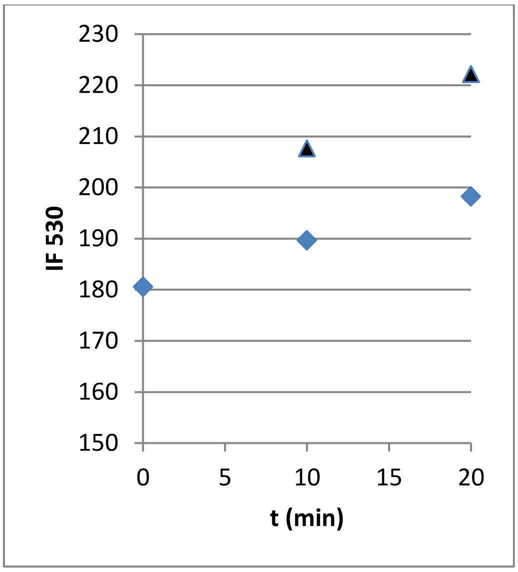

Figure 43. PA waves effect on LUVs BS values obtained of emission IF530 with excitation at 450 nm
Laser energies of 100 mJ/cm^2 (▲) during 10 and 20 minutes; controls, no PA waves application (blue)

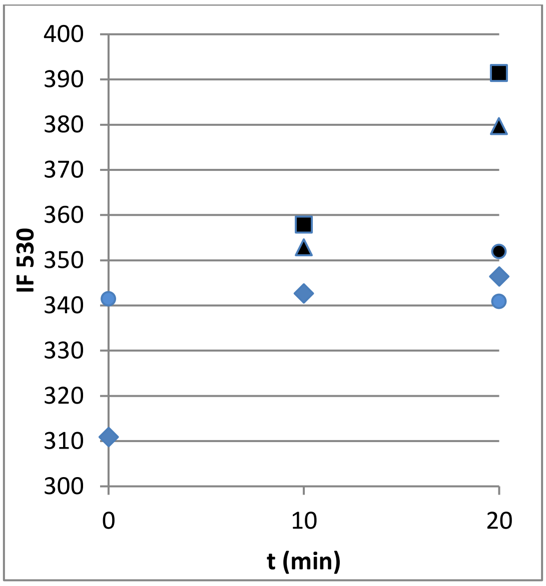

Figure 44. PA waves effect on LUVs AD values obtained of emission IF530 with excitation at 450 nm
Laser energies of 100 mJ/cm^2 (▲) and 200 mJ/cm^2 (■) during 10 and 20 minutes; using cover glass set-up (•) controls, no PA waves application (blue)

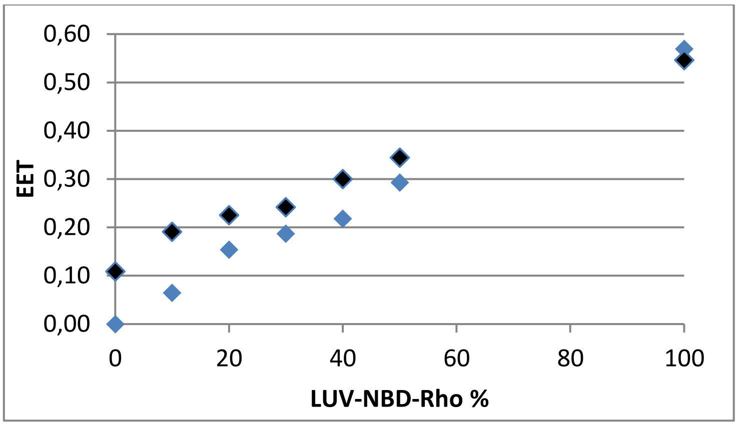

Figure 45. EET values obtained for LUVs AD (blue) and LUVs BS (black) with different percentages of LUV-NBD-Rho

3.3. Permeability of LUVs

The release of Fluorescein (F) from inside the LUVs was followed by the increase in fluorescence that goes along with its dilution into the aqueous media outside the LUVs. The percentage of F that has permeated is given by Equation (8),

$$\%\ Release = \frac{IF(t)-IF(0)}{IF(\infty)-IF(0)} \text{x } 100\% \qquad (9),$$

where IF(t) is the fluorescence intensity at time t, If(0) the initial fluorescence intensity (which corresponds to the fluorescence right after the dilution of LUVs) and IF(∞) the maximum fluorescence (obtained by adding TX to the cuvette).

The kinetics curves obtained at different temperatures (figure 46) were adjusted firstly with a mono-exponential function, due to considering the fluorophores mechanism of release as a first order reaction,

$$F_{in} \xrightarrow{k} F_{out}$$

where F_{in} represents the molecules encapsulated inside LUVs and F_{out} being the molecule after release from LUVs. Knowing that the disappearing rate of F_{in} and consequent appearing of F_{out} is given by

$$\frac{dF_{in}}{dt} = -k[F_{in}]$$

$$\int_0^t \frac{dF_{in}}{F_{in}} = \int_0^t -kdt$$

$$\ln(F_{in}) = -kt + \ln(IF_0)$$

where If_0 is the initial intensity of F_{in} when t = 0 and k is the rate constant of fluorescein release to the external medium, the mono-exponential function for F_{out} is obtained by

$$F_{out} = If_0(1 - e^{-kt})$$

from

$$F_{in} = F_{in_0}e^{-kt}$$

and

$$F_{out} = If_0 - F_{in}$$

It was noted that this mono-exponential time dependence could not describe adequately the results, so a new bi-exponential fit was applied,

$$\%\, F_{out} = a_1\left(1 - e^{-k_1 t}\right) + a_2\left(1 - e^{-k_2 t}\right) \tag{10}$$

where a_2 corresponds to the percentage of release during the slower moment, a_1 of the faster, k_1 is the constant rate of the fast release and k_2 of the slower release. The values obtained are displayed in table 14.

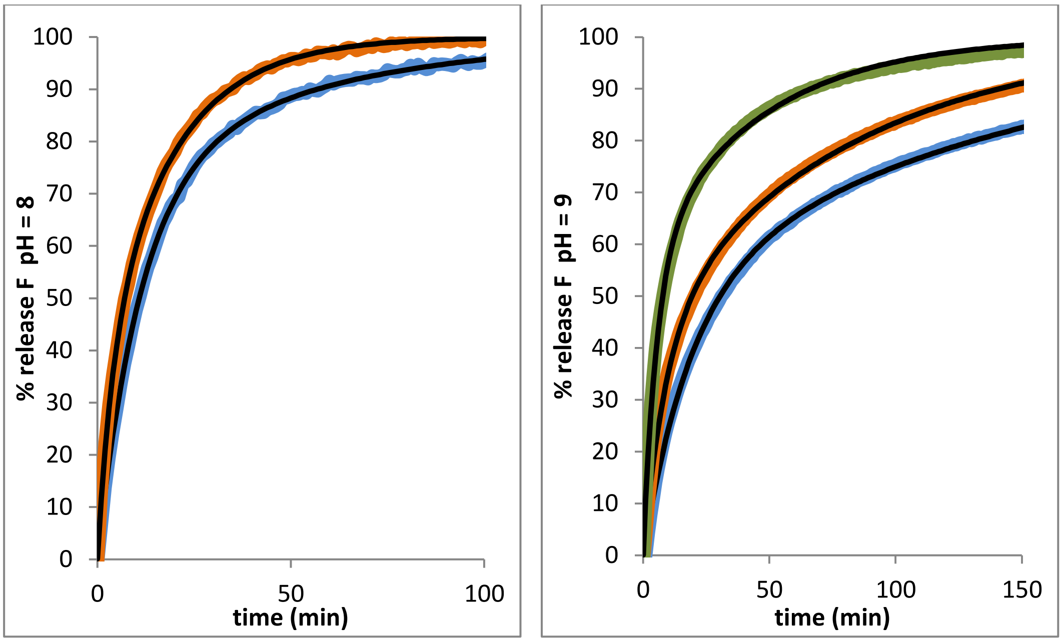

Figure 46. Kinetics of fluorescein release at pH = 8 (left) and pH = 9 (right) at 15 (blue), 25 (orange) and 35°C (green)

Table 14. Rate constants k1 and k2 (min-1), weight of each moment (%) and t(1/2) (calculated time at 50% of release, in minutes) obtained for the release of fluorescein from LUVs

T (°C)	pH = 8					pH = 9				
	k_1	a_1	k_2	a_2	$t_{\frac{1}{2}}$	k_1	a_1	k_2	a_2	$t_{\frac{1}{2}}$
15	0.09	72.45	0.019	27.55	10.8	0.05	50.09	0.01	49.91	30.5
25	0.27	66.03	0.08	33.97	3.6	0.11	43.10	0.012	56.90	19.4
35						0.18	57.27	0.022	42.73	7.7

The release of fluorescein is pH dependent, being faster at pH=8. At pH=9, the fluorescein is completely in the dianionic form, while at pH=8, a significant fraction of the mono-negative form exists (pKa_3=6.43),[71] so the permeability is slower at pH=9. Naturally, at a physiological pH the permeation would be faster so a way to slow down its rate would be adding a group of high molecular weight.

3.3.1 Synthesis of fluorescein derivative

The glucose acetylation (figure 47) was successfully confirmed by ^{1}H and ^{13}C NMR.

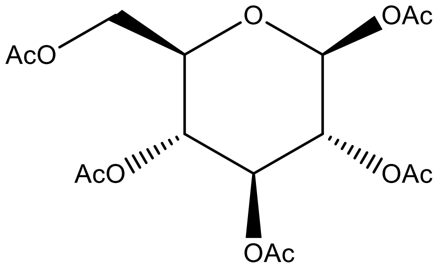

Figure 47. 2,3,4,6-Tetra-O-acetyl-beta-D-glucose (1.1)

^{1}H NMR (400 MHz, $CDCl_3$): δ (ppm) 6.35, 6.34, 5.51, 5.49, 5.46, 5.18, 5.16, 5.13, 5.12, 5.11, 5.10, 4.30, 4.29, 4.27, 4.26, 4.15, 4.14, 4.13, 4.12, 4.10, 4.09, 2.20, 2.11, 2.06, 2.04, 2.03.

^{13}C NMR (101 MHz, $CDCl_3$): δ (ppm) 170.62, 170.22, 169.65, 169.39, 168.74, 89.07, 69.82, 69.19, 67.89, 61.45, 20.87, 20.69, 20.66, 20.56, 20.44.

The presence of 5 singlets with intensity of 3 in the ^{1}H NMR and 5 peaks around 170 ppm in the ^{13}C NMR shows the presence of 5 acetyl groups.

Fluorescein reactions that produced precipitates **2.1** to **2.4** had similar retention factors compared to fluorescein, which indicated that the reactions had not been successful. The reactions that produced compounds **2.5** amd **2.6** demonstrated by TLC different fluorescent spots other than the fluorescein, but were difficult to understand what product was formed by NMR due to the complexity and superposition of the peaks. The desired compound that would result of the addition of ethanolamine to the fluorescein would be reflected by 2 new triplets (by ^{1}H NMR) and 2 new peaks (by ^{13}C NMR). HPLC was then used to evaluate the products existing in those precipitates (figure 48).

HPLC chromatographs were obtained using the a gradient eluent based literature (Chinese Journal of Pharmaceutical Analysis, Volume 28, Number 6, 1 2008) starting with acetonitrile at 20% and H_2O:Net3 (119:1) 80% alternating to 80%:20% until 10 minutes and maintaining this eluent until 12 minutes and from 12 to 14 minutes the proportions return to 20%:80%. The chromatograph (figure 51) shows that, besides de fluorescein peak there are other fluorescently detected peaks at different time retentions in both 2.5 and 2.6 samples, that should be separated in the future. Due to time restrictions, work followed with FITC-dextran.

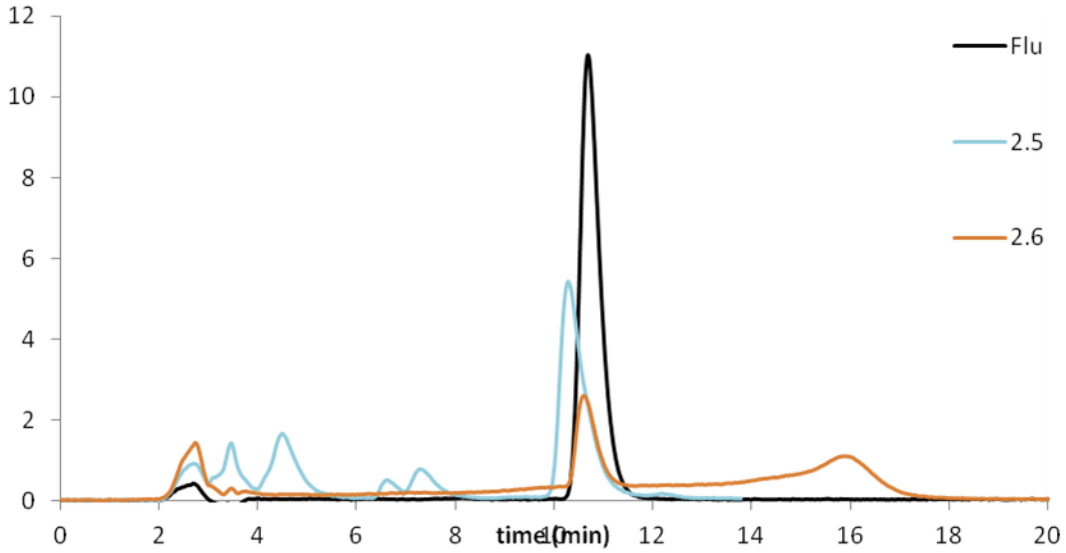

Figure 48. HPLC chromatographs of products 2.5 and 2.6

3.4. PA waves effect on GUVs

As GUVs were chosen not only because of the size similarity with cells, but also due to the fact they're bigger than large vesicles, the effect of photoacoustic waves, using different laser fluencies and times can be seen via microscopy.

In a first experiment, a mixture of GUV-NBD and GUV-Rho was submitted to PA waves (figure 49).

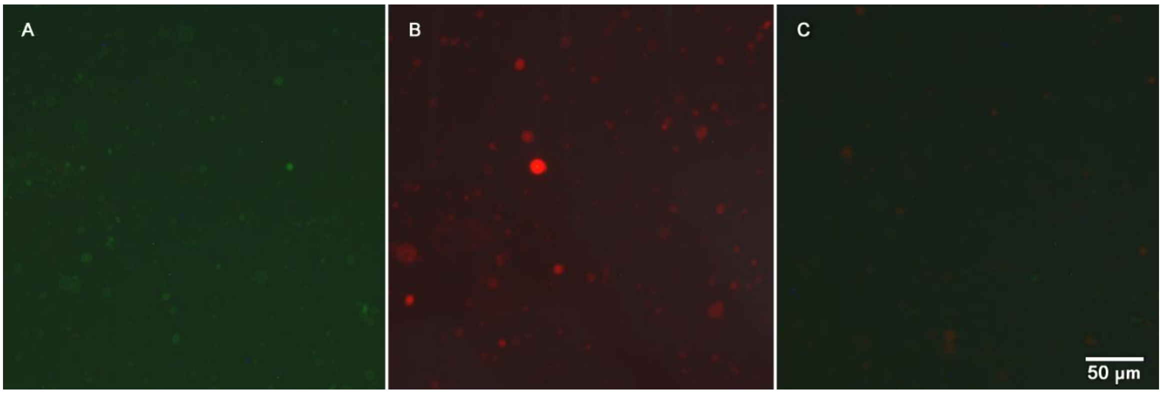

Figure 49. A. blue channel. B. green channel. C. After PA waves application (40 mJ/cm2 10 minutes) using blue channel light source

It was observed that photoacoustic waves with this fluency maintain GUVs size and GUV-Rho can be seen using blue light excitation source. This result could demonstrate FRET after the PA waves application, however other fluencies should be tested.

New GUVs (hydrated with FITC-dextran sucrose solution diluted 50 times with glucose solution and collected from the pellet) were subjected to different conditions (figure 50). The sample was placed on the top of the irradiation setup (figure 15 of the Materials and Methods section) and maintained for different times with the laser at different energies. After the experiment, the sample was removed from the irradiation setup and placed on a 96 well plate. All pictures were obtained 2h after GUVs deposited on the plate. The lipid bilayer of GUVs was observed using the green light source (left column) that detected rhodamine's fluorescence and contrast between the aqueous media inside and outside the GUVs was evaluated using the blue light source (right column) that detected the fluorescence of FITC-dextran. Control (sample without contact with the setup) showed GUVs with majority of sizes approximately between 10 and 20 µm.

Applying laser energy of 100 mJ/cm^2 during 10 minutes, GUVs seem to maintain their size and the contrast is still very similar to the control. However, applying the PA waves for 20 minutes, GUVs are visibly smaller and there is very little contrast between GUVs and the external medium. There's a noticeable tendency of getting smaller when increasing the laser fluency and exposure time, with 200 mJ/cm^2 applied during 10 minutes GUVs are visibly smaller than compared to those at the same time but lower laser fluency. The contrast is lower comparing to the same time of application.

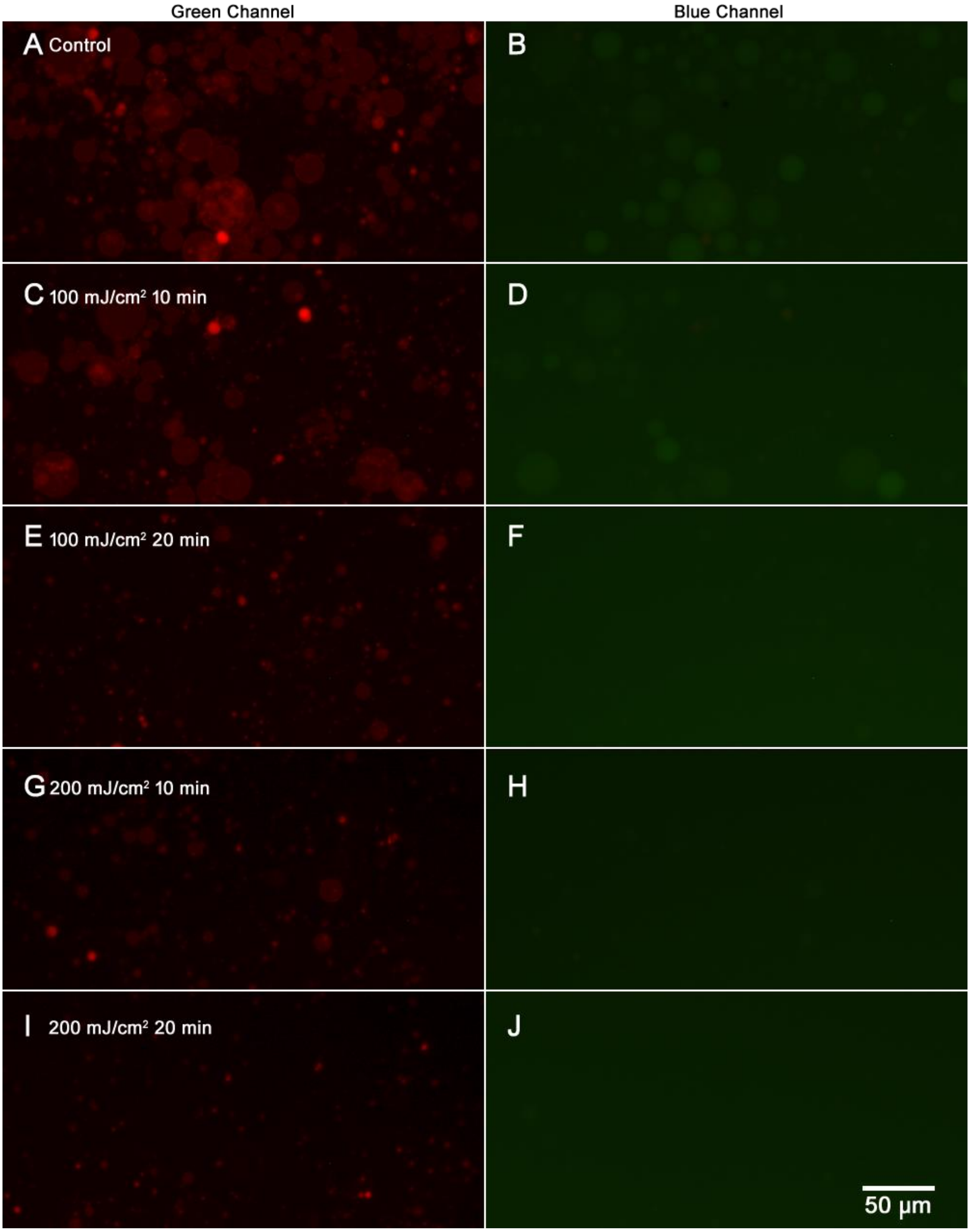

Figure 50. PA waves effect on GUVs

A,B: Control (no PA waves); C,D: 10 minutes with 100mJ/cm^2 energy; E,F: 20 minutes, 100 mJ/cm^2; G,H: 10 minutes 200 mJ/cm^2; I,J: 20 minutes 200 mJ/cm^2.

The loss of contrast is due to FITC-dextran originally inside the GUVs leaking into the external medium. This leakage may be caused by the PA waves application because without the PA waves, FITC-dextran release from vesicles is very slow because of its large size and negative charge, meaning that the permeabilization of the membrane is slow.

Another observation is that, taking in account GUVs intrinsic fragility, they resist to PA waves application with 100 mJ/cm^2 laser energy.

Two main reasons that could explain GUVs becoming smaller are: fission (such happens during cell division where the content of the cell is kept inside the membrane) and disassembly/destruction of the membrane.

Data showed that the contrast lost between GUVs and the outer medium could be explained by destruction of the membrane by PA waves. The formed fragments will tend to reassemble in smaller vesicles with internal content equilibrated with the external media.

This concludes that there is effect by the application of PA waves in the lipid components of the membrane. Further studies would need to be done for better understanding of the mechanism by which they are affected.

Chapter 4:

Final remarks

The permeability of biological membranes is a subject of constant study. And with this work, GUVs and LUVs were used as biomimetic models for the understanding of the PA waves effects in the lipid components of the biological membranes.

There was an evident effect of the PA waves application on GUVs properties but a quantitative study with more laser fluencies should be done in the future. New lipid compositions and hydration solutions could also be tested in order to compare GUVs stability upon PA waves application. Vesicle fusion could be tested using LUVs and GUVs mixtures in order to mimic a drug delivery system closer to the cells. The effect in LUVs was not observed, nonetheless, further experiments using laser pulses of picoseconds should be tried.

The synthesis of fluorescein linked to ethanolamine via several reactions showed the existence of fluorescent compounds. Separation and characterization steps would have to be taken.

Chapter 5:

Bibliography

(1) Sá, G. F. F. Photoacoustic Waves for Transdermal Drug Delivery, Universidade de Coimbra, 2012.

(2) Sá, G. F. F.; Serpa, C.; Arnaut, L. G. Stratum Corneum Permeabilization with Photoacoustic Waves Generated by Piezophotonic Materials. *J. Control. Release* **2013**, *167*, 290–300.

(3) Weinberger, A.; Tsai, F. C.; Koenderink, G. H.; Schmidt, T. F.; Itri, R.; Meier, W.; Schmatko, T.; Schröder, A.; Marques, C. Gel-Assisted Formation of Giant Unilamellar Vesicles. *Biophys. J.* **2013**, *105* (1), 154–164.

(4) Yeagle, P. L. *The Structure of Biological Membranes*, 3rd ed.; CRC Press, 2011.

(5) Stryer, L.; Berg, J. M.; Tymoczko, J. L. *Biochemistry*, 5th ed.; W. H. Freshman and Company: New York, 2002.

(6) Vereb, G.; Szollosi, J.; Matko, J.; Nagy, P.; Farkas, T.; Vigh, L.; Matyus, L.; Waldmann, T. A.; Damjanovich, S. Dynamic, yet Structured: The Cell Membrane Three Decades after the Singer-Nicolson Model. *Proc. Natl. Acad. Sci.* **2003**, *100* (14), 8053–8058.

(7) Gennis, R. B. *Biomembranes: Molecular Structure and Function*; Springer Science + Business Media: New York, 1989.

(8) Lehninger, A. L. *Principles of Biochemistry*, 7th ed.; Cox, M. M., Nelson, D. L., Eds.; W. H. Freeman and Company: New York, 2017.

(9) Vaz, W. *Wiley Encyclopedia of Chemical Biology*; John Wiley & Sons, Inc., 2008.

(10) Hjort Ipsen, J.; Karlström, G.; Mourtisen, O. G.; Wennerström, H.; Zuckermann, M. J. Phase Equilibria in the Phosphatidylcholine-Cholesterol System. *Biochim. Biophys. Acta* **1987**, *905*, 162–172.

(11) Eeman, M.; Deleu, M. From Biological Membranes to Biomimetic Model Membranes. *BASE [Online]* **2010**, *14* (4), 719–736.

(12) Ikeda, M.; Kihara, A.; Igarashi, Y. Lipid Asymmetry of the Eukaryotic Plasma Membrane: Functions and Related Enzymes. *Biol. Pharm. Bull.* **2006**, *29* (8), 1542–1546.

(13) Sand, S. L.; Nissen-Meyer, J.; Sand, O.; Haug, T. M. Plantaricin A, a Cationic Peptide Produced by Lactobacillus Plantarum, Permeabilizes Eukaryotic Cell Membranes by a Mechanism Dependent on Negative Surface Charge Linked to Glycosylated Membrane Proteins. *Biochim. Biophys. Acta - Biomembr.* **2013**, *1828* (2), 249–259.

(14) Goñi, F. M.; Alonso, A.; Bagatolli, L. A.; Brown, R. E.; Marsh, D.; Prieto, M.; Thewalt, J. L. Phase Diagrams of Lipid Mixtures Relevant to the Study of Membrane Rafts. *Biochim. Biophys. Acta* **2008**, *1781*, 665–684.

(15) Seu, K. J.; Cambrea, L. R.; Everly, R. M.; Hovis, J. S. Influence of Lipid Chemistry on Membrane Fluidity: Tail and Headgroup Interactions. *Biophys. J.* **2006**, *91* (10), 3727–3735.

(16) Tien, H. T.; Ottova-Leitmannova, A. Fundamental Aspects of Biological Membranes. In *Membrane Biophysics*; Elsevier: Amsterdam and New York, 2000; Vol. Volume 5, pp 23–82.

(17) Kinnunen, P. K. J.; Kõiv, A.; Lehtonen, J. Y. A.; Rytömaa, M.; Mustonen, P. Lipid Dynamics and Peripheral Interactions of Proteins with Membrane Surfaces. *Chem. Phys. Lipids* **1994**, *73*, 181–207.

(18) Zimmerberg, J.; Chernomordik, L. V. Membrane Fusion. *Adv. Drug Deliv. Rev.* **1999**, *38* (3), 197–205.

(19) De Gier, J.; Mandersloot, J. G.; Van Deenen, L. L. M. Lipid Composition and Permeability of Liposomes. *Biochim. Biophys. Acta* **1968**, *150*, 666–675.

(20) McLaughlin, S. The Electrostatic Properties of Membranes. *Annu. Rev. Biophys. Biophys. Chem.* **1989**, *18* (1), 113–136.

(21) Kaszuba, M.; Corbett, J.; Watson, F. M.; Jones, A. High-Concentration Zeta Potential Measurements Using Light-Scattering Techniques. *Philos. Trans. R. Soc.* **2010**, *368* (1927), 4439–4451.

(22) Honary, S.; Zahir, F. Effect of Zeta Potential on the Properties of Nano-Drug Delivery Systems - A Review (Part 1). *Trop. J. Pharm. Res.* **2013**, *12* (2), 255–264.

(23) Ropert, C. Liposomes as a Gene Delivery System. *Brazilian J. Med. Biol. Res.* **1999**, *32* (2), 163–169.

(24) Shinoda, W. Permeability across Lipid Membranes. *Biochim. Biophys. Acta - Biomembr.* **2016**, *1858* (10), 2254–2265.

(25) Chernomordik, L. V.; Kozlov, M. M. Mechanics of Membrane Fusion. *Nat. Struct. Mol. Biol.* **2008**, *15* (7), 675–683.

(26) Fan, Z. A.; Tsang, K. Y.; Chen, S. H.; Chen, Y. F. Revisit the Correlation between the Elastic Mechanics and Fusion of Lipid Membranes. *Sci. Rep.* **2016**, *6* (300), 1–10.

(27) Yeagle, P. L. *The Membranes of Cells*, 3rd ed.; Elsevier, 2016.

(28) Costa, A. P.; Xu, X.; Burgess, D. J. Freeze-Anneal-Thaw Cycling of Unilamellar Liposomes: Effect on Encapsulation Efficiency. *Pharm. Res.* **2014**, *31* (1), 97–103.

(29) Struck, D. K.; Hoekstra, D.; Pagano, R. E. Use of Resonance Energy Transfer To Monitor Membrane Fusion. *Biochemistry* **1981**, *20*, 4093–4099.

(30) Loura, L. M. S.; Prieto, M. FRET in Membrane Biophysics: An Overview. *Front. Physiol.* **2011**, *2*, 1–11.

(31) Chivers, C. E.; Koner, A. L.; Lowe, E. D.; Howarth, M. How the Biotin–streptavidin Interaction Was Made Even Stronger: Investigation via Crystallography and a Chimaeric Tetramer. *Biochem. J.* **2011**, *435*, 55–63.

(32) Matos, C.; Moutinho, C.; Lobão, P. Liposomes as a Model for the Biological Membrane: Studies on Daunorubicin Bilayer Interaction. *J. Membr. Biol.* **2012**, *245* (2), 69–75.

(33) Moreno, M. J.; Estronca, L. M. B. B.; Vaz, W. L. C. Translocation of Phospholipids and Dithionite Permeability in Liquid-Ordered and Liquid-Disordered Membranes. *Biophys. J.* **2006**, *91* (3), 873–881.

(34) Allen, T. M.; Cullis, P. R. Liposomal Drug Delivery Systems: From Concept to Clinical Applications. *Adv. Drug Deliv. Rev.* **2013**, *65* (1), 36–48.

(35) Saffari, M.; Reza, H.; Dass, C. R. Barriers to Liposomal Gene Delivery : From Application Site to the Target. **2016**, *15* (February), 3–17.

(36) Hope, M. J.; Bally, M. B.; Webb, G.; Cullis, P. R. Production of Large Unilamellar Vesicles by a Rapid Extrusion Procedure. Characterization of Size Distribution,

Trapped Volume and Ability to Maintain a Membrane Potential. *BBA - Biomembr.* **1985**, *812* (1), 55–65.

(37) Uhumwangho, M. U.; Okor, R. S. Current Trends in the Production and Biomedical Applications of Liposomes: A Review. *J. Med. Biomed. Res.* **2005**, *4* (1), 9–21.

(38) Rodriguez, N.; Pincet, F.; Cribier, S. Giant Vesicles Formed by Gentle Hydration and Electroformation: A Comparison by Fluorescence Microscopy. *Colloids Surfaces B Biointerfaces* **2005**, *42*, 125–130.

(39) Stein, H.; Spindler, S.; Bonakdar, N.; Wang, C.; Sandoghdar, V. Production of Isolated Giant Unilamellar Vesicles under High Salt Concentrations. *Front. Physiol.* **2017**, *8*, 1–16.

(40) Lasic, D. D.; Papahadjopoulos, D. *Medical Applications of Liposomes*; Elsevier, 1998.

(41) Lipinski, C. A. Lead- and Drug-like Compounds: The Rule-of-Five Revolution. *Drug Discov. Today Technol.* **2004**, *1* (4), 337–341.

(42) Aschi, M.; D'Archivio, A. A.; Fontana, A.; Formiglio, A. Physicochemical Properties of Fluorescent Probes: Experimental and Computational Determination of the Overlapping PKaValues of Carboxyfluorescein. *J. Org. Chem.* **2008**, *73* (9), 3411–3417.

(43) Hinow, P.; Radunskaya, A.; Tucker, I.; Yang, L. Kinetics of Bile Salt Binding to Liposomes Revealed by Carboxyfluorescein Release and Mathematical Modeling. *J. Liposome Res.* **2012**, *22* (3), 237–244.

(44) Lee, S.; Anderson, T.; Zhang, H.; Flotte, T. J.; Doukas, A. G. Alteration of Cell Membrane by Stress Waves in Vitro. *Ultrasound Med. Biol.* **1996**, *22* (9), 1285–1293.

(45) Doukas, A. G.; Flotte, T. J. Physical Characteristics and Biological Effects of Laser-Induced Stress Waves. *Ultrasound i n Med. Biol.* **1996**, *22* (2), 151–164.

(46) Mulholland, S. E.; Lee, S.; McAuliffe, D. J.; Doukas, A. G. Cell Loading with Laser-Generated Stress Waves. *Pharmaceutical Research*. 1999, pp 514–518.

(47) Doukas, A. G.; Kollias, N. Transdermal Drug Delivery with a Pressure Wave. *Adv. Drug Deliv. Rev.* **2004**, *56* (5), 559–579.

(48) Hutchins, D. A. Ultrasonic Generation by Pulsed Lasers. In *Physical Acoustics*; Academic Press, Inc., 1988; Vol. 18, pp 21–123.

(49) Yao, C. P.; Zhang, Z. X.; Rahmanzadeh, R.; Huettmann, G. Laser-Based Gene Transfection and Gene Therapy. *IEEE Trans. Nanobioscience* **2008**, *7* (2), 111–119.

(50) Silva, A. D.; Serpa, C.; Arnaut, L. G. *Photoacoustic Waves for Gene Therapy*.

(51) Sánchez, D.; Johnson, N.; Li, C.; Novak, P.; Rheinlaender, J.; Zhang, Y.; Anand, U.; Anand, P.; Gorelik, J.; Frolenkov, G. I.; et al. Noncontact Measurement of the Local Mechanical Properties of Living Cells Using Pressure Applied via a Pipette. *Biophys. J.* **2008**, *95* (6), 3017–3027.

(52) Zhang, Z.; Wang, Y.; Zhang, H.; Tang, Z.; Liu, W.; Lu, Y.; Wang, Z.; Yang, H.; Pang, W.; Zhang, H.; et al. Hypersonic Poration: A New Versatile Cell Poration Method to Enhance Cellular Uptake Using a Piezoelectric Nano-Electromechanical Device. *Small* **2017**, *13* (18), 1–10.

(53) Silva, G. B. da; Guimarães, B. M.; Assis, S. P. O.; Lima, V. L. M.; Oliveira, R. N. de. Ultrasound-Assisted Synthesis of 1- N -β-D-Glucopyranosyl-1 H -1,2,3-Triazole Benzoheterocycles and Their Anti-Inflammatory Activities. *J. Braz. Chem. Soc.* **2013**, *24* (6), 914–921.

(54) Xu, W.; Park, J. Y.; Kattel, K.; Ahmad, M. W.; Bony, B. A.; Heo, W. C.; Jin, S.; Park, J. W.; Chang, Y.; Kim, T. J.; et al. Fluorescein-Polyethyleneimine Coated Gadolinium Oxide Nanoparticles as T1magnetic Resonance Imaging (MRI)-Cell Labeling (CL) Dual Agents. *RSC Adv.* **2012**, *2*, 10907–10915.

(55) Chen, R. F.; Knutson, J. R. Mechanism of Fluorescence Concentration Quenching of Carboxyfluorescein in Liposomes: Energy Transfer to Nonfluorescent Dimers. *Anal. Biochem.* **1988**, *172*, 61–77.

(56) de la Maza, A.; Parra, J. L. Alterations in Phospholipid Bilayers Caused by Sodium Dodecyl Sulphate / Triton X-1O0 Mixed Systems. *Colloid Polym. Sci.* **1996**, *274* (3), 253–260.

(57) Serpa, C.; Schabauer, J.; Piedade, A. P.; Monteiro, C. J. P.; Pereira, M. M.; Douglas, P.; Burrows, H. D.; Arnaut, L. G. Photoacoustic Measurement of Electron Injection Efficiencies and Energies from Excited Sensitizer Dyes into Nanocrystalline TiO2films. *J. Am. Chem. Soc.* **2008**, *130*, 8876–8877.

(58) Sá, G. F. F.; Serpa, C.; Arnaut, L. G. Mechanisms of Interaction between Very High-Frequency Photoacoustic Waves and the Skin. *Optics in Health Care and Biomedical Optics V*, **2012**, *8553*, 85531Z.

(59) Domingues, M. M.; Santiago, P. S.; Castanho, M. A.; Santos, N. C. What Can Light Scattering Spectroscopy Do for Membrane-Ctive Peptide Studies. *J. Pept. Sci.* **2008**, *14*, 394–400.

(60) Stetefeld, J.; McKenna, S. A.; Patel, T. R. Dynamic Light Scattering: A Practical Guide and Applications in Biomedical Sciences. *Biophys. Rev.* **2016**, *8*, 409–427.

(61) Chirio-Lebrun, M.-C.; Prats, M. Fluorescence Resonance Energy Transfer (FRET): Theory and Experiments. *Biochem. Educ.* **1998**, *26*, 320–323.

(62) Sahoo, H. Förster Resonance Energy Transfer - A Spectroscopic Nanoruler: Principle and Applications. *J. Photochem. Photobiol. C Photochem. Rev.* **2011**, *12*, 20–30.

(63) Kuscu, M.; Akan, O. B. Coverage and Throughput Analysis for FRET-Based Mobile Molecular Sensor/Actor Nanonetworks. *Nano Commun. Netw.* **2014**, *5*, 45–53.

(64) Loura, L. M. S.; de Almeida, R. F. M.; Silva, L. C.; Prieto, M. FRET Analysis of Domain Formation and Properties in Complex Membrane Systems. *Biochim. Biophys. Acta* **2009**, *1788*, 209–224.

(65) Loura, L. M. S.; Fernandes, F.; Prieto, M. Membrane Microheterogeneity: Förster Resonance Energy Transfer Characterization of Lateral Membrane Domains. *Eur. Biophys. J.* **2010**, *39* (4), 589–607.

(66) Lakowicz, J. R. *Topics in Fluorescence Spectroscopy, Volume 2: Principles*; Kluwer Academic Publishers, 2002; Vol. 2.

(67) Schaufele, F.; Demarco, I.; Day, R. N. FRET Imaging in the Wide-Field Microscope. In *Molecular Imaging*; Periasamy, A., Day, R. N., Eds.; 2005; pp 72–94.

(68) Becker, W.; Bergmann, A.; Biscotti, G. L.; Rueck, A. Advanced Time-Correlated Single Photon Counting Techniques for Spectroscopy and Imaging in Biomedical Systems. **2004**, *5340*, 104.

(69) Pina, J.; De Melo, J. S.; Burrows, H. D.; Macanita, A. L.; Galbrecht, F.; Bunnagel, T.; Scherf, U. Alternating Binaphthyl-Thiophene Copolymers: Synthesis, Spectroscopy, and Photophysics and Their Relevance to the Question of Energy Migration versus Conformational Relaxation. *Macromolecules* **2009**, *42* (5), 1710–1719.

(70) Striker, G.; Subramaniam, V.; Seidel, C. A. M.; Volkmer, A. Photochromicity and Fluorescence Lifetimes of Green Fluorescent Protein. *J. Phys. Chem. B* **1999**, *103* (40), 8612–8617.

(71) Sjbaöck, R.; Nygren, J.; Kubista, M. Absorption and Fluorescence Properties of Fluorescein. *Spectrochim. Acta Part A* **1995**, *51*.

(72) Leikin, S.; Parsegian, V. A.; Rau, D. C.; Rand, R. P. Hydration Forces. *Annu. Rev. Phys. Chem.* **1993**, *44*, 369–395.

(73) Siegel, D. P.; Epand, R. M. The Mechanism of Lamellar-to-Inverted Hexagonal Phase Transitions in Phosphatidylethanolamine: Implications for Membrane Fusion Mechanisms. *Biophys. J.* **1997**, *73*, 3089–3111.

(74) Cardoso, R. M. S.; Filipe, H. A. L.; Gomes, F.; Moreira, N. D.; Vaz, W. L. C.; Moreno, M. J. Chain Length Effect on the Binding of Amphiphiles to Serum Albumin and to POPC Bilayers. *J. Phys. Chem. B* **2010**, *114*, 16337–16346.